

JGR Solid Earth

RESEARCH ARTICLE

10.1029/2021JB022857

Key Points:

- We determine the first 3-D radially anisotropic model for the crust and uppermost mantle of central and West Antarctica
- Resolution of shallow structure reveals >4 km of sediment beneath the Ross Ice Shelf, but limited sediment thickness for interior basins
- The shallowest crust and uppermost mantle generally show positive radial anisotropy, anisotropy in the mid-tolower crust is highly variable

Supporting Information:

Supporting Information may be found in the online version of this article.

Correspondence to:

Z. Zhou, zhou.z@wustl.edu

Citation:

Zhou, Z., Wiens, D. A., Shen, W., Aster, R. C., Nyblade, A., & Wilson, T. J. (2022). Radial anisotropy and sediment thickness of West and Central Antarctica estimated from Rayleigh and Love wave velocities. *Journal of Geophysical Research: Solid Earth*, 127, e2021JB022857. https://doi. org/10.1029/2021JB022857

Received 27 JUL 2021 Accepted 9 FEB 2022

Author Contributions:

Conceptualization: Zhengyang Zhou, Douglas A. Wiens

Data curation: Zhengyang Zhou, Douglas A. Wiens, Weisen Shen, Richard C. Aster, Andrew Nyblade, Terry J. Wilson

Funding acquisition: Douglas A. Wiens **Methodology:** Zhengyang Zhou, Weisen Shen

Project Administration: Douglas A. Wiens

Software: Zhengyang Zhou, Weisen Shen Supervision: Douglas A. Wiens Writing – original draft: Zhengyang Zhou

Writing – review & editing: Douglas A. Wiens, Weisen Shen, Richard C. Aster, Andrew Nyblade

© 2022. American Geophysical Union. All Rights Reserved.

Radial Anisotropy and Sediment Thickness of West and Central Antarctica Estimated From Rayleigh and Love Wave Velocities

Zhengyang Zhou¹, Douglas A. Wiens¹, Weisen Shen², Richard C. Aster³, Andrew Nyblade⁴, and Terry J. Wilson⁵

¹Department of Earth and Planetary Sciences, Washington University in St Louis, St Louis, MO, USA, ²Department of Geosciences, Stony Brook University, Stony Brook, NY, USA, ³Department of Geosciences and Warner College of Natural Resources, Colorado State University, Fort Collins, CO, USA, ⁴Department of Geosciences, Penn State University, University Park, PA, USA, ⁵School of Earth Sciences, Ohio State University, Columbus, OH, USA

Abstract Many recent Antarctic seismic structure studies use Rayleigh wave data and thus determine only the SV structure. Love waves provide greater resolution for shallow structure, and coupled with Rayleigh waves, can constrain radial anisotropy by comparing vertically (V_{SV}) and horizontally (V_{SH}) polarized shear velocities. In this study, we jointly analyze Rayleigh and Love wave phase and group velocities from ambient noise to develop a new radially anisotropic velocity model for West and Central Antarctica with an improved shallow crustal resolution using all broadband data collected in Antarctica over the past 20 years. Group and phase velocity maps for Rayleigh and Love waves are estimated and inverted for shear wave velocity structure using a Monte Carlo method. We determine a new sediment distribution map that reveals a thick sedimentary basin (~4 km) beneath the Southeastern Ross Embayment. Sediment thicknesses at interior basins such as the Polar Subglacial Basin and Bentley Subglacial Trench are modest (<1.5 km), suggesting that these basins are sediment-starved. The shallow crust as well as the mid-to-lower crust in several places shows strong positive anisotropy $(V_{SH} > V_{SV})$, likely due to lattice preferred orientation of mica-bearing rocks. However, large regions of the mid-to-lower crust show negative anisotropy, likely due to lattice preferred orientation of plagioclase. The uppermost mantle is characterized by strong positive radial anisotropy (4%–8%) in West Antarctica, with the largest anisotropy beneath the Transantarctic and Whitmore Mountains, likely resulting from horizontal olivine preferred orientation due to tectonic activity.

Plain Language Summary The crust and upper mantle structure of Antarctica have been poorly understood until recent studies, due to the remote location and thick ice cover. Seismic anisotropy, the directional dependence of seismic wave propagation, represents a probe to understand the deformation history of the crust and mantle. In this study, we use all broadband seismic records collected in Antarctica over the past 20 years to investigate the shear wave radial anisotropy structure. In addition, the improved shallow resolution allows us to determine a new continental-scale sediment thickness map, which reveals a thick sediment layer beneath the Southeastern Ross Embayment. Basins on the interior of the continent show limited sediment cover, likely due to sediment-starved conditions through much of their history. We find positive anisotropy ($V_{SH} > V_{SV}$) in the shallow crust and a few places in the mid-to-lower crust, likely due to the orientation of the mica-bearing rocks. Much of the lower crust shows negative anisotropy ($V_{SH} < V_{SV}$), likely due to the lattice preferred orientation of plagioclase. The uppermost mantle generally has positive anisotropy, with the largest magnitudes beneath the Transantarctic and Whitmore Mountains, where it likely results from the tectonic activity.

1. Introduction

With the improvement of seismic station coverage in Antarctica during the past 20 years, a number of different seismic studies, using body wave tomography (Hansen et al., 2014; Lloyd et al., 2013; Lucas, Soto, et al., 2020; Watson et al., 2006; White-Gaynor et al., 2019), teleseismic and ambient noise Rayleigh wave tomography (An et al., 2015; Graw et al., 2016; Heeszel et al., 2013, 2016; Lawrence et al., 2006b; O'Donnell et al., 2019; Pyle et al., 2010; Shen, Wiens, Anandakrishnan, et al., 2018), seismic attenuation (Lawrence et al., 2006c), receiver functions (Chaput et al., 2014; Emry et al., 2015; Finotello et al., 2011; Hansen et al., 2010; Lawrence et al., 2006a; Ramirez et al., 2016, 2017) and shear wave splitting (Accardo et al., 2014; Barklage et al., 2009;

ZHOU ET AL. 1 of 23



Graw & Hansen, 2017) have revealed new details of Antarctica crustal and upper mantle structure. These studies have mapped principal features such as Moho depth and mantle velocity variations, but shallower details such as the distribution and thickness of sedimentary basins have not been as extensively studied due to the limited resolution of the upper crustal structure. In addition, previous surface and body wave tomography studies have focused on the isotropic structure or have determined only the SV structure from Rayleigh waves. The joint use of both Love and Rayleigh waves from ambient noise data can better resolve the shear wave velocity structure of the crust, as well as improve general constraints on and interpretation of the radial anisotropic structure of Antarctica.

The amplitude and orientation of seismic anisotropy reveal aspects of the deformation history of the crust and mantle (Long & Silver, 2009) that are essential for a better understanding of continental tectonics and stress distribution in the lithosphere. Compared with crustal anisotropy, mantle anisotropy has been relatively well studied in both lab experiments and seismological observations and can generally be explained by the lattice preferred orientation (LPO) of anisotropic minerals such as olivine and possible shape preferred orientation (SPO) of melt or layer flow (Becker et al., 2008; Ferreira et al., 2019; Karato et al., 2008; Long & Becker, 2010; Long & Silver, 2009). However, crustal anisotropy, which is essential to understand the evolution of the crust and orogenic process, is less explored and explained. Due to compositional heterogeneity and the presence of several different highly anisotropic minerals in the crust, both LPO and SPO may play a role in crustal anisotropy. The alignment of anisotropic crustal minerals, such as mica and amphiboles, caused by extension or uplift, is often proposed as the reason for observed middle to lower crustal anisotropy (Barberini et al., 2007; Moschetti et al., 2010b; Xie et al., 2013). SPO is caused by layered structures as well as the distribution of microcracks, faults, and melt pockets (Dalton & Gaherty, 2013; Dreiling et al., 2018; Illsley-Kemp et al., 2019) in the crust can also cause the observed anisotropy.

Seismic studies are unable to completely resolve the general (21-parameter) elasticity tensor, describing seismic velocity as a function of propagation direction. Tractable parameterizations approximate anisotropy as either azimuthal, with seismic velocities varying with horizontal propagation direction, or radial, corresponding to a transverse isotropic (TI) medium. For radial anisotropy, there is symmetry around a vertical axis, and there are two shear wave velocities for horizontal propagation wave, V_{SH} (horizontally polarized) and V_{SV} (vertically polarized). The anisotropy amplitude is defined as the percentage difference between V_{SH} and V_{SV} as calculated from $\frac{V_{SH}-V_{SV}}{V_{Voigt}}$, where V_{Voigt} is the isotropic shear wave velocity given by:

$$V_{Voigt} = \sqrt{\frac{V_{SH}^2 + 2V_{SV}^2}{3}} \tag{1}$$

Since Rayleigh wave and Love waves are sensitive to V_{SV} and V_{SH} respectively, the Rayleigh-Love wave discrepancy, characterized by the inability to fit both Love and Rayleigh wave dispersion curves with an isotropic velocity structure, indicates that the anisotropic parameters should be introduced so that the Love and Rayleigh wave dispersion curves can be simultaneously fit to obtain the radially anisotropic velocity structure. Several studies have successfully used Love and Rayleigh wave dispersion curves from ambient noise tomography to determine crustal and uppermost mantle radial anisotropy, including Western US (Moschetti et al., 2010b), Canada (Dalton & Gaherty, 2013), Northeast China (Guo et al., 2016), Tibet and Himalaya (Guo et al., 2012; Xie et al., 2013) and the Alaska region (Feng & Ritzwoller, 2019).

The use of both Rayleigh and Love waves from ambient noise also provides better constraints on shallow crustal structure, compared to Rayleigh waves alone, as shown by the sensitivity kernels (Figure 1). Improved constraints on shallow structure allow for estimation of the total sediment thickness, which is poorly constrained for Antarctica. Sediment thickness provides important constraints on paleotopographic reconstruction, basin evolution, erosion history, and other near-surface processes (Lindeque et al., 2016; Wobbe et al., 2014). Other continents generally show thick sedimentary sequences in interior basins, such as the 4 km-thick Michigan Basin and 5 km-thick Illinois basin in the continental US (Howell & van der Pluijm, 1999), but it is unclear whether some interior Antarctic basins also contain sediments. Love and Rayleigh wave ambient noise tomography offers the opportunity to constrain sediment thickness across Antarctica, as demonstrated by Feng and Ritzwoller (2019), who mapped sedimentary basin thicknesses up to 6 km in Alaska.

ZHOU ET AL. 2 of 23



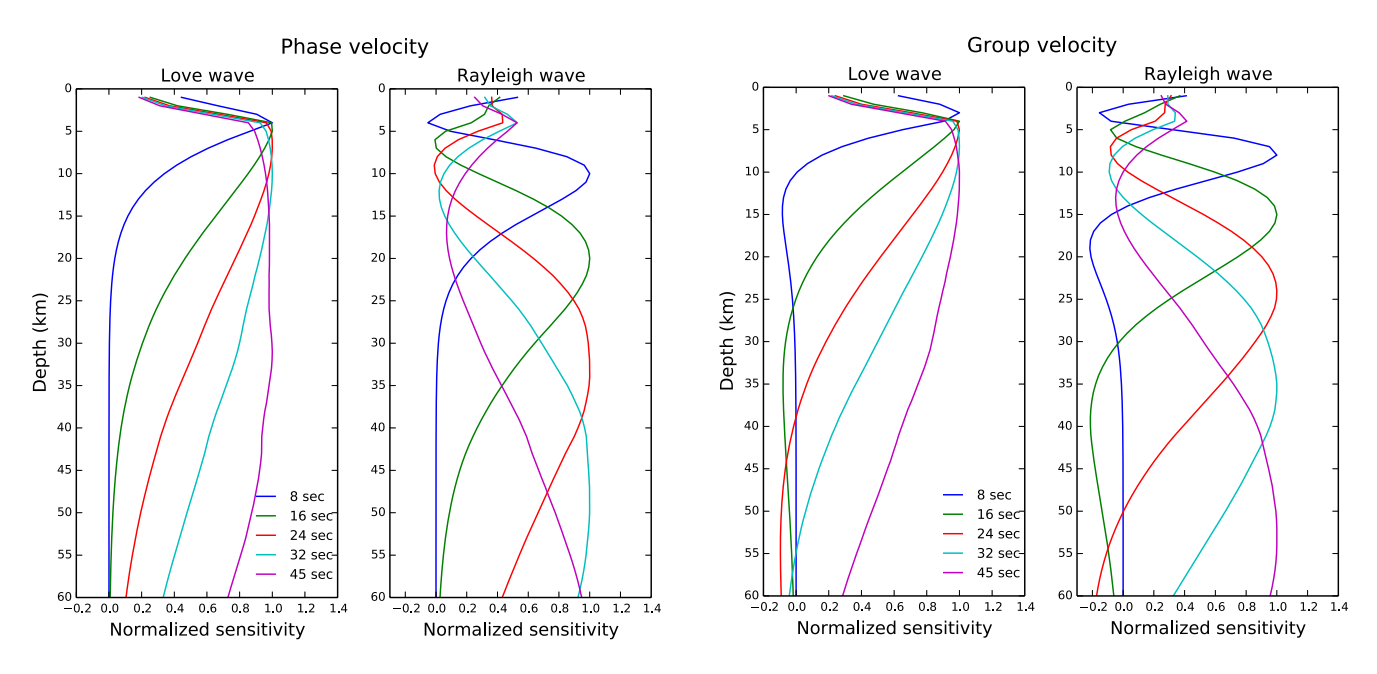


Figure 1. Sensitivity kernels of Rayleigh and Love waves for different periods. Phase velocity is shown on the left and group velocity on the right. The kernels are calculated based on the average 1-D Voigt average velocity from the final model of this study. (An enlarged version for upper 20 km is shown at Figure S9 in Supporting Information S1).

In this study, we present the first 3-D radially anisotropic shear wave velocity model for the crust and uppermost mantle beneath West and central Antarctica. We use both Rayleigh (8–50 s) and Love (8–40 s) wave group

and phase velocity from ambient noise tomography to construct this model. The dispersion curves are inverted for radial anisotropic structure using a full transverse-isotropic formulation, without approximations. We also take advantage of the short-period Love waves' high sensitivity to the shallow structure and obtain the first continental-scale sediment thickness map of Antarctica and discuss the implications for the geological history of this continent.

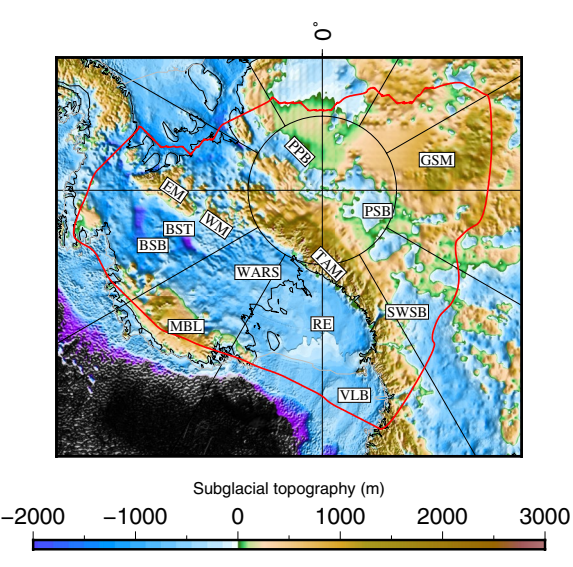


Figure 2. The bedrock topography of Antarctica from BEDMAP2 (Fretwell et al., 2012) with geological features. Red line encloses the study region. Abbreviations: GSM - Gamburtsev Subglacial Mountains, PSB - Polar Subglacial Basin, TAM - Transantarctic Mountains, RE - Ross Embayment, MBL - Marie Byrd Land, EM - Ellsworth Mountains. WM – Whitmore Mountains, VLB – Victory Land Basin, SWSB – South Wilkes Subglacial Basin, PPB – Pensacola-Pole Basin, BST – Bentley Subglacial Basin, WARS – West Antarctic Rift System, and BSB – Byrd Subglacial Basin.

2. Geological and Geophysical Setting

Antarctica is generally divided into two principal geographic regions, separated by the Transantarctic Mountains (TAM). West Antarctica (WA) has been tectonically active during the Mesozoic and Cenozoic, whereas East Antarctica (EA) is geologically much older and represents one of the major fragments of the Gondwana supercontinent (Figure 2). WA is comprised of several smaller tectonic blocks, including the West Antarctic Rift System (WARS), Marie Byrd Land (MBL), Ellsworth-Whitmore Mountains (EM and WM), and the Antarctic Peninsula. The WARS is characterized by Cretaceous to Cenozoic extension from the Ross Embayment (RE) to the Byrd Subglacial Basin. Extension occurred in several phases, with initial extension along the entire WARS (Siddoway, 2007) giving way to more focused late Cenozoic extension in the RE region (Huerta & Harry, 2007; Wilson & Luyendyk, 2006). The WARS crust is thin as a result of the history of crustal extension; the average thickness is about 25 km, but the thinnest part, in the RE region, is less than 20 km (Chaput et al., 2014; Ramirez et al., 2016, 2017; Shen, Wiens, Anandakrishnan, et al., 2018). However, plate kinematic models (Granot & Dyment, 2018) and recent GPS results

ZHOU ET AL. 3 of 23



show no evidence of current extension, and present geodetic velocities are dominated by glacial isostatic adjustment (Barletta et al., 2018). MBL is a region of high topography adjacent to and north of the WARS with extensive Cenozoic volcanism (LeMasurier, 1990), and ongoing magmatic-attributed seismicity (Lough et al., 2013). MBL volcanism has been proposed to result from a deep mantle or plume source (Wörner, 1999). The EM and WM comprise a small block considered to be a fragment of the EA craton that separated during Gondwana break-up and rotated into WA (Jordan et al., 2017, 2020; Randall & Niocaill, 2004).

The TAM is a 3500 km-long extensional mountain range at the boundary between West and East Antarctica, with elevations up to 4,500 m. Thermochronology shows several episodes of uplift, beginning in the Cretaceous and continuing through much of the Cenozoic (Fitzgerald, 2002). The orogenic process and precise chronology of TAM uplift are still poorly constrained, with several possible models proposed (Bialas et al., 2007; ten Brink & Stern, 1992; Goodge et al., 2001; Huerta & Harry, 2007; Stern & Brinkten, 1989). Recent seismic tomography results (Shen, Wiens, Stern, et al., 2018) indicate that mountain building in the southern TAM involved the removal of the lithosphere and replacement with a hot buoyant mantle, but magnetotelluric results from the central TAM indicate a simpler model with intact lithosphere beneath the mountains (Wannamaker et al., 2017), suggesting significant along-strike variation.

The regions of EA included in this study are generally thought to represent an Archean to Proterozoic craton with an affinity with Australian cratonic terrains (Boger, 2011). The most notable tectonic feature is the Gamburtsev Subglacial Mountains (GSM), which is poorly understood due to a complete absence of surface rock exposures. The age and origin of GSM are widely debated (Ferraccioli et al., 2011; Heeszel et al., 2013; Lloyd et al., 2013). Detrital zircon studies suggest an absence of major tectonic activity within the East Antarctic interior for the past 520 Ma (Flierdt et al., 2008), thus implying that the GSM is at least of this age.

Sedimentary basins in the marine regions surrounding Antarctica have been studied using marine active source seismology. For example, total sediment thicknesses of greater than 8 km have been found for parts of the Victoria Land Basin in the Ross Embayment (ANTOSTRAT, 1995; Lindeque et al., 2016). However, little is known about the geological setting and sediment infill of the deep topographic basins in the Antarctic interior due to their remote locations and absence of rock outcrop. The Bentley Trench and Byrd Basin, two exceptionally (~2 km) deep topographic basins in West Antarctica, may have formed as rift basins during the WARS extension (Bingham et al., 2012; T. A. Jordan et al., 2010). The Southern Wilkes Basin, Polar Subglacial Basin (South Pole Basin), and Pensacola-Pole Basin (Paxman et al., 2019) comprise an almost continuous band of low topography spanning 300–600 km onto the East Antarctic Craton from the TAM, with having an as yet unclear origin.

Recent seismological studies, reviewed in Wiens et al. (2021), have determined the structure of the crust and uppermost mantle throughout much of Antarctica. EA is characterized by thick crust (35–55 km) and fast cratonic mantle lithosphere, whereas WA has a thinner crust (20–35 km) and slower upper mantle velocities. A few studies have also investigated the seismic anisotropy of Antarctica. Ritzwoller et al. (2001) found 1%–5% positive $(V_{SH} > V_{SV})$ radial anisotropy in the Antarctic uppermost mantle, with somewhat stronger anisotropy in WA compared to EA, but was unable to resolve smaller features. O'Donnell et al. (2019) carried out a regional study and found lateral variations in crustal radial anisotropy across parts of WA, including positive radial anisotropy in the lower crust near EM, WM, and part of WARS. They attributed the crustal anisotropy to the lattice preferred orientation of anisotropic minerals, such as mica and amphibole, aligned by extension. Teleseismic shear wave splitting studies find strong azimuthal anisotropy, interpreted as resulting from upper mantle lattice preferred orientation, across parts of WA and the TAM (Accardo et al., 2014; Barklage et al., 2009; Graw & Hansen, 2017). However, there are no previous comprehensive studies of crustal and uppermost mantle radial anisotropy for the study area.

3. Data and Analysis

3.1. Seismic Stations in Antarctica

In this study, we analyze continuous data from all publicly available broadband seismic stations deployed on the Antarctica continent, including the Antarctic Peninsula, from 2000 to 2018. These 218 stations include six large temporary networks (TAMSEIS (Lawrence et al., 2006b); AGAP/GAMSEIS (Hansen et al., 2010); POLENET/ANET (Lloyd et al., 2015); TAMNET (Hansen et al., 2015); RIS/DRIS (Bromirski et al., 2015) and UKANET

ZHOU ET AL. 4 of 23

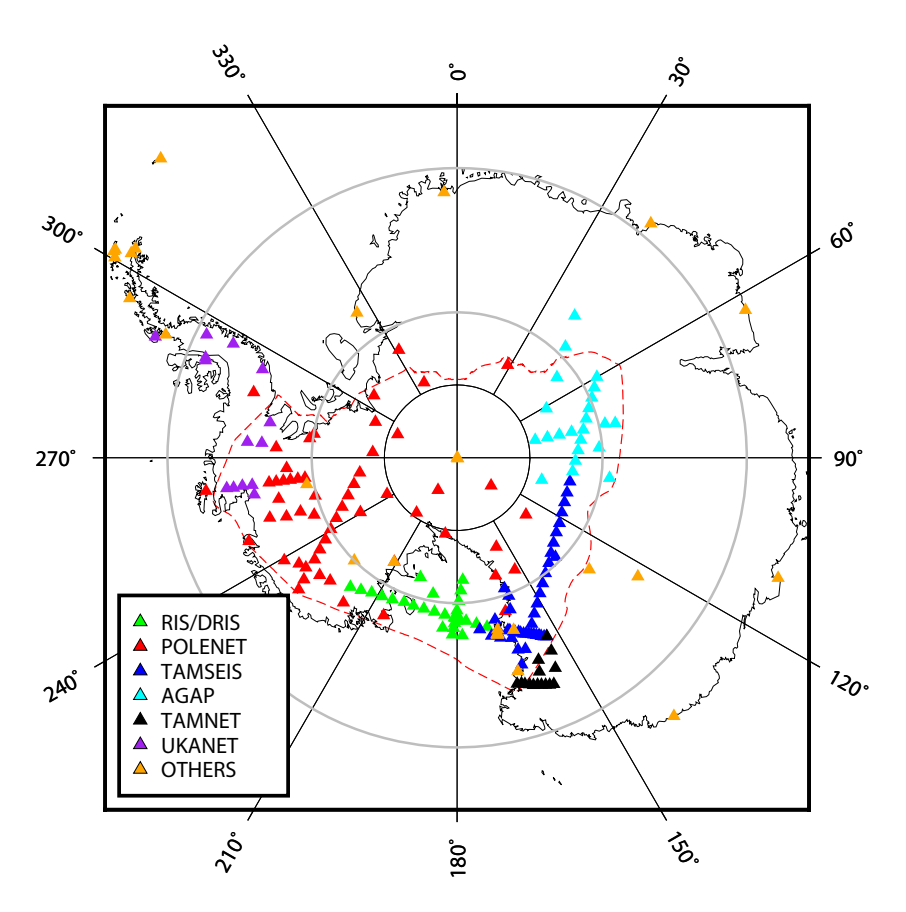


Figure 3. Seismic stations used in this study, with major deployments and networks indicated. Deployment abbreviations and references given in the text. Dotted line encloses the study region.

(O'Donnell et al., 2019)), several smaller deployments of isolated stations associated with other international networks south of -60° latitude, and all Global Seismographic Network stations in Antarctica. The data from all stations are used in the Rayleigh wave data processing. However, there are 29 stations in the RIS/DRIS network that were located on the floating Ross Ice Shelf for which the water layer makes it impossible to extract Love wave signals, so the total number of stations used in the Love wave analysis is 189. Station coverage is shown in Figure 3.

3.2. Group and Phase Velocity Measurements From Ambient Noise

The ambient noise cross-correlation (CC) method has proven to be a powerful method to obtain surface wave signals from simultaneously deployed seismic station pairs by many studies (e.g., Lin et al., 2007, 2008; Shen, Ritzwoller, & Schulte-Pelkum, 2013). We apply a modification of the procedure described in Bensen et al. (2007) to all station pairs to obtain Love and Rayleigh group and phase velocity dispersion curves using the ambient noise field of Antarctica (Anthony et al., 2015). To retrieve both Rayleigh and Love wave CC data, we cut three-component records into 1-day long time series, then calculate cross-correlations between each of the six auto-and cross-component component pairs for the Z, N, and E components following time and frequency domain normalization. Rayleigh wave phase and group velocity can be obtained from linear stacked daily Z-Z cross-correlations by applying automated frequency-time analysis (Dziewonski et al., 1969; Ritzwoller & Levshin, 1998). We obtained phase and group velocity measurements of Rayleigh waves at periods from 8 to 55 s for each station pair.

The Love wave measurements require cross-correlation of N-E, N-N, E-E, and E-N component pairs to form the transverse-transverse correlation (Lin et al., 2008). However, the lower signal-to-noise ratio (SNR) for horizontal

ZHOU ET AL. 5 of 23



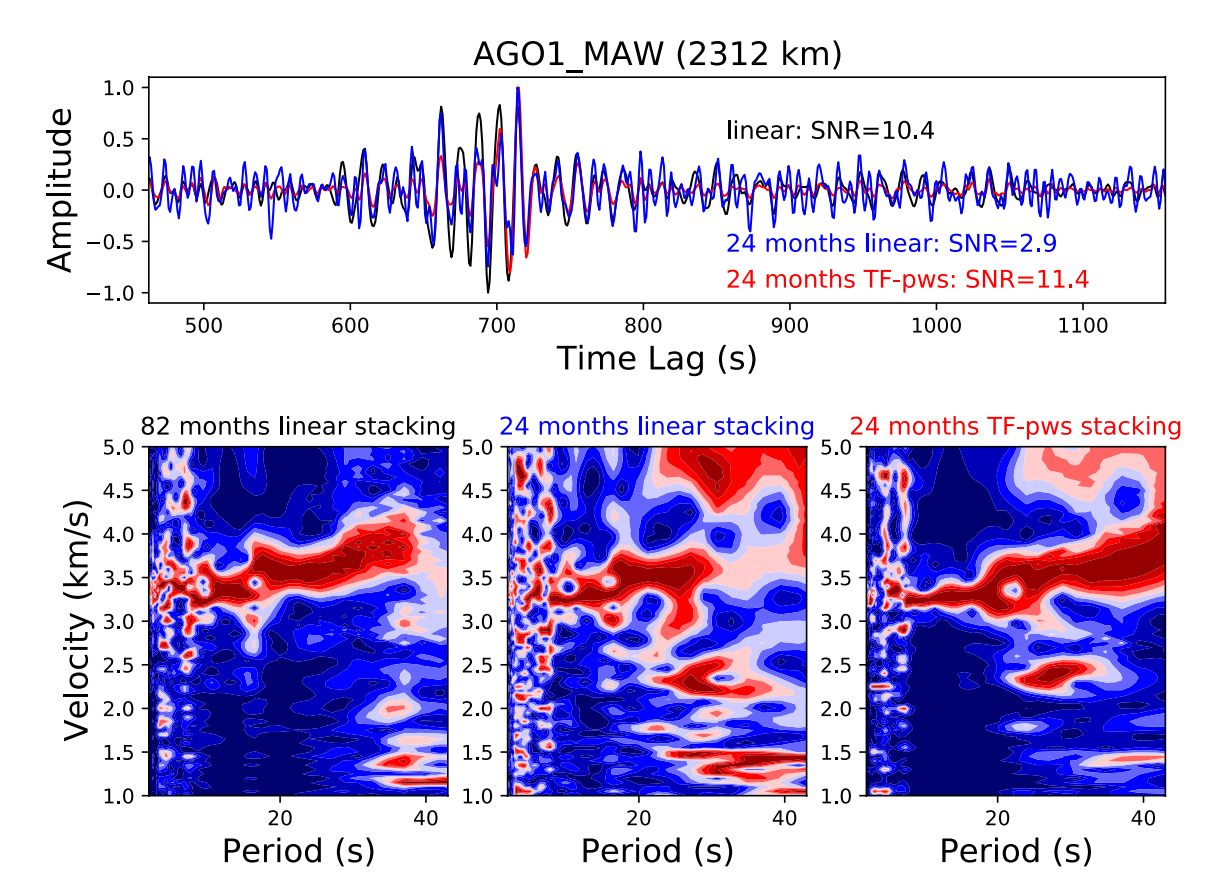


Figure 4. Comparison between linear stacking for 24 and 82 months of stacked data and Time-frequency phase-weighted stacking (TF-PWS) for 24 months of data. The top panel shows the waveforms from the three different stacking results. The bottom panel shows multiple filter plots of spectral amplitude as a function of group velocity and period, with red denoting high spectral amplitude. TF-PWS allows good results to be obtained at long periods even if only shorter duration records are available.

cross-correlations yields fewer high-quality measurements, particularly at periods greater than 30 s. To improve the Love waves SNR, we linearly stack the daily CC into monthly estimates and apply the time-frequency phase weighted stacking (TF-pws) method (Li et al., 2018; Schimmel & Gallart, 2007; Schimmel & Paulssen, 1997) to stack these monthly records. By applying this stacking method combined with standard processing, we found that the Love wave phase and group velocities could be extracted at periods between 8 and 40 s, compared with 8–30 s from only linear-stacking. This is important since the longer period Love waves are critical for constraining the lower crust and uppermost mantle anisotropy structure. We found that applying the TF-pws stacking method at least doubles the SNR from linear stacking and increases the number of useable Love wave phase velocity measurements from 1093 to 6249 at periods between 30 and 40 s.

Because it is a non-linear stacking method, TF-pws may introduce some nonlinear distortion into the CC waveforms. However, compared with other coherence-enhancing stacking methods such as nth root stacking (Kanasewich et al., 1973) and phase-weighted stacking (Schimmel & Paulssen, 1997), the distortion from TF-pws is smaller (Li et al., 2018). We also tested the reliability of the measurements made using the TF-pws processing. From previous studies, the longer the recording time available for a given station pair, the better the SNR that can be obtained after stacking (Sabra et al., 2005). Thus, using different stacking time periods allowed us to gauge SNR improvement and also compare the results with linear stacking results. We choose a path with a relatively long recording time and compared the result from three different stacking approaches: 1. Linear stacking all the data (82 months); 2. Linear stacking of 24 months of data; 3. TF-pws stacking of 24 months of data. As shown in Figure 4, the SNR of the 24-month TF-pws is improved compared to the 24-month linear stacking, and the group and phase velocity measurements are similar to those obtained from the linear stack using all 82 months of data. We conclude that TF-pws processing enhances the signal without problematic artifacts, and note that it

ZHOU ET AL. 6 of 23



produces good velocity estimates when applied to 24-month horizontal component data sets, which is a common deployment time for many of the temporary seismic stations in Antarctica.

3.3. Tomography and Uncertainty Estimates

We apply three quality and residual criteria for our group and phase velocity measurements based on station distance, SNR, and the misfit of the tomography result, to cull unreliable data. First, we require the distance between station pairs to be larger than three wavelengths for short period and two wavelengths for a longer period (>30 s) to satisfy the far-field approximation and thus acquire a consistent, clear surface wave measurement. Second, the SNR must be larger than 10 for Rayleigh waves and 8 for Love waves. The SNR criteria are slightly smaller for Love waves to ensure we obtain a reasonable number of Love wave measurements, noting that the SNR is typically lower for Love waves. The third criterion was applied iteratively for outlier recognition during the initial tomographic inversion. We first inverted for a highly smoothed phase velocity map for each period to create a reference dispersion curve for phase velocity. Then we apply frequency-time analysis to both Rayleigh and Love data using the appropriate reference dispersion curves. This step can improve the results by addressing some cycle skipping in the measurements. We then carry out successive tomographic iterations, with the smoothing reduced in each subsequent inversion, requiring every measurement to be within three standard deviations of the predicted value. This iterative criterion for data culling prevents outlier measurements from introducing extreme velocity structures in the phase and group velocity maps.

For polar regions, the latitude-longitude grid does not map to quasi-equally-spaced grid nodes, which is critical for the equant parameterization of the tomographic inversion. We create a new coordinate system using the inverse Vincenty equation (Vincenty, 1975) to get the highly accurate distance and azimuth from the South Pole to all stations and project the station into a great circle referenced coordinate system with the South Pole at (0, 0). After this coordinate conversion, the maximum change in distance between two stations relative to that calculated using geographic coordinates is less than 200 m, which is smaller than corresponding measurement errors of phase and group velocity. After the velocity structure inversion, we convert back to the original geographic coordinate system.

We use a straight-ray based tomography method (Barmin et al., 2001) to determine the phase and group velocities for each period on a 0.5° by 0.5° grid for both Rayleigh and Love waves. After determining optimal inversion regularization using L-curve analysis (Hansen, 1999), we obtain the Love wave group and phase velocity at a period range of 8–40 s and Rayleigh wave results for 8–55 s. The total number of unique ambient noise paths used is about 3500 for Love and 8000 for Rayleigh waves. For longer periods, we additionally incorporate the Rayleigh wave phase velocities obtained by two-plane wave earthquake tomography by Heeszel et al. (2016). These longer period data do not help to constrain the anisotropy structure directly, as periods greater than 55 s have limited sensitivity at the shallower depths studied in this paper (Figure 1). However, by ensuring that the deeper mantle structure is realistic, the resolution of the shallow structure in our inversion is improved.

Figure 5 shows examples of the phase velocity maps for Rayleigh and Love waves at 8 and 35 s. The 8-s maps dominantly reflect the velocity in the uppermost ~12 km, including the ice and sediment layers, as indicated by the sensitivity kernels (Figure 1). The Ross Embayment shows particularly low velocity at this period for both Love and Rayleigh waves. At 35 s, the Raleigh wave sensitivity kernel peaks at depths of approximately 30–60 km, and the major resolved features are crustal thickness and uppermost mantle velocity variations. To check our data coverage ability, a set of checkboard tests for different periods were processed. The results indicate a reasonable recovery (Figures S1 and S2 in Supporting Information S1).

Local dispersion curve uncertainty provides a critical constraint for the formal uncertainty of velocity structure, and is essential for weighting in the Bayesian Monte-Carlo inversion method. Here we adapt the method of Shen, Ritzwoller, Kang, et al. (2016) to determine dispersion curve uncertainties. For phase velocity uncertainties, we first assume a standard deviation of 0.01 km/s for the node where the path density is sufficient (as described below), and use this number as the reference point for all periods, based on previous studies and the agreement between phase velocities from ambient noise and earthquake Rayleigh waves (Shen, Wiens, Anandakrishnan, et al., 2018). Then we estimate uncertainties for all the nodes and periods using the following empirical equation:

ZHOU ET AL. 7 of 23



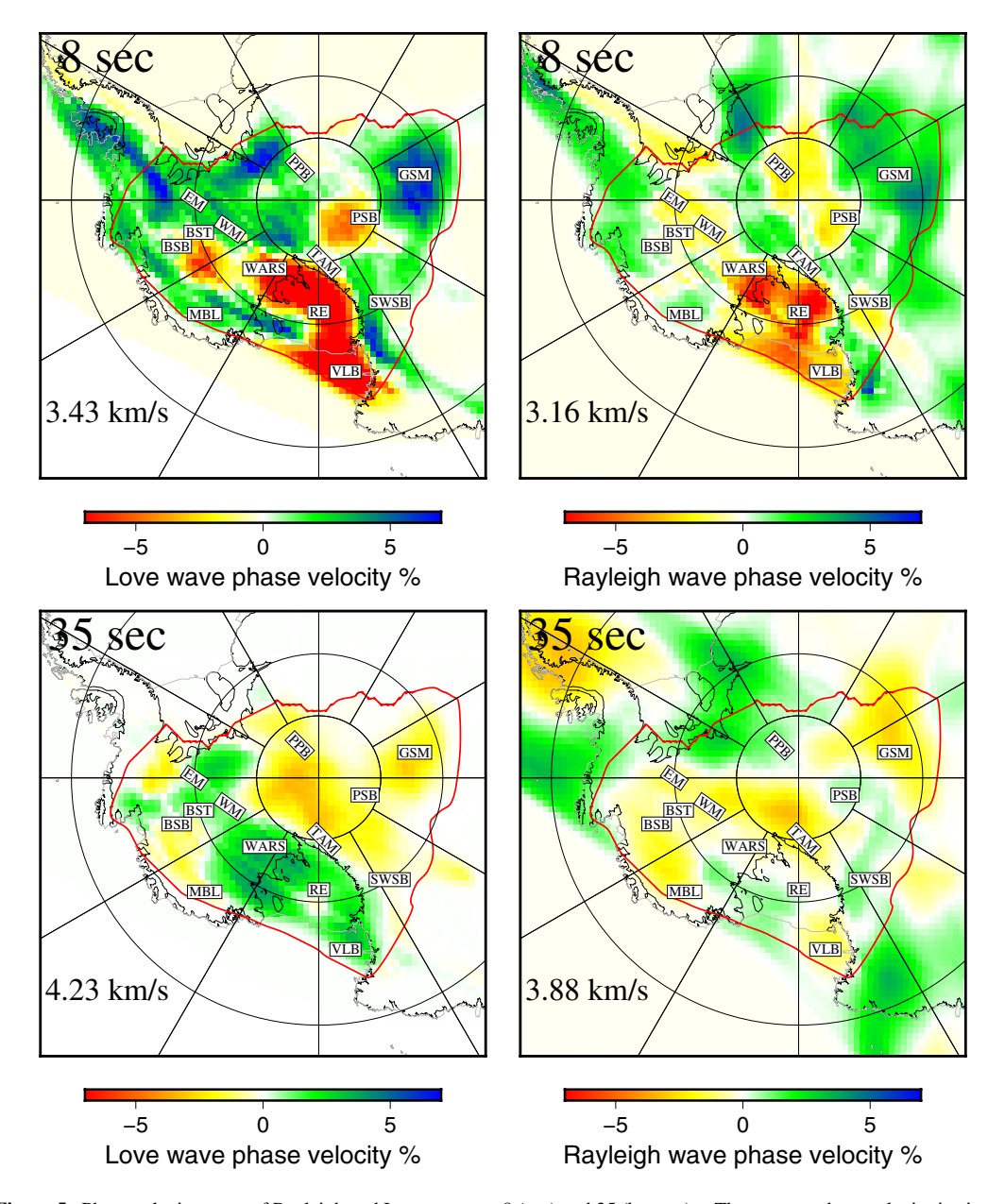


Figure 5. Phase velocity maps of Rayleigh and Love waves at 8 (top) and 35 (bottom) s. The average phase velocity is given in the lower left corner of each figure. Abbreviations are the same as in Figure 2.

$$\sigma(r) = \left(\frac{R(r)}{R_{ref}}\right)^k \sigma_{ref} \tag{2}$$

where σ_{ref} and R_{ref} are the uncertainty and path density for a reference grid point, respectively, R(r) is the path density for a given point, k is an empirical constant (from 1.0–1.1) and $\sigma(r)$ is the estimated uncertainty. The definition of sufficient path density is different for Rayleigh and Love waves. Since there is a significant difference in the number of paths, we use 400 paths per 2,500 km² as the high path density criterion for Love waves and 600 paths per 2,500 km² for Rayleigh waves to ensure similar weighting of each data set in the velocity inversion. For group velocity uncertainties, we scaled the uncertainties from the phase velocity estimates by a factor of two, as suggested by previous studies using similar methods (Moschetti et al., 2010a; Shen & Ritzwoller, 2016).

ZHOU ET AL. 8 of 23



4. Shear Wave Velocity and Radial Anisotropy Inversion

In this section, we describe the procedure used to invert Rayleigh and Love wave phase and group velocity dispersion curves to obtain a 3-D shear wave velocity and radial anisotropy structure. The 3-D structure is determined on a grid with 0.5° spacing by inverting the phase and group velocities determined for each node to obtain the structure at depth. First, we discuss the model parameterization and then describe the Bayesian Monte Carlo inversion algorithm for the anisotropic medium, which is adapted from a similar method described in Shen, Ritzwoller, Schulte-Pelkum, and Lin (2013). The Monte Carlo inversion offers the advantages of providing a detailed sampling of the prior model space, the generation of a posterior model with maximum posterior parameter estimates, and associated formal uncertainties.

4.1. Model Parametrization

For a transversely isotropic (TI) medium, the five independent elastic moduli in the stiffness matrix are commonly denoted by the parameters A, C, L, N, and F. The relationships between moduli and seismic velocity are:

$$A = \rho V_{PH}^2; \quad C = \rho V_{PV}^2; L = \rho V_{SV}^2; N = \rho V_{SH}^2; F = \eta (A - 2L)$$
(3)

where ρ is density, V_{PH} and V_{PV} are the velocities of horizontally and vertically propagating P-waves, V_{SH} and V_{SV} are velocities of horizontally and vertically polarized S waves, and η controls the seismic velocity oblique along the symmetry axis and the shape of shear wave speed surface. We assume that anisotropy in the crust and mantle are dominated by shear wave anisotropy so that $V_{PH} = V_{PV}$ and F = A - 2L, the same as for an isotropic medium. We impose this condition because surface wave velocities are only weakly dependent on P wave velocities and because previous studies indicate that this assumption has a negligible effect on estimating shear wave crust and mantle anisotropy from surface waves (Xie et al., 2013). Since both Rayleigh and Love wave velocities are mostly sensitive to the shear velocity, other parameters are linked to the shear wave velocity in the inversion. To constrain density and V_P in the crust, we use empirical relationships to V_S adapted from Brocher (2005). In the mantle, we assume a constant V_P/V_S ratio of 1.789, which is based on AK135 (Kennett et al., 1995) at 120 km depth, to constrain V_P . The mantle density is constrained by increasing density by 10 kg/m³ per 1% velocity change. The attenuation structure is taken from the 1-D profile of PREM (Dziewonski & Anderson, 1981) for the crust and fixed to $Q_S = 150$ and $Q_P = 300$ for the uppermost mantle.

For most locations in Antarctica, the 1-D profile is parameterized as a four-layer structure with three discontinuities, consisting of ice or water, sediment, crust, and mantle from the surface to 300 km. For the ice layer (assumed isotropic in the inversion), the thickness and velocity are fixed. The large-scale ice thickness is now known fairly well throughout most of Antarctica from ice-penetrating radar, so we fix the thickness using the values provided by Bedmap2 (Fretwell et al., 2012) with the shear velocity of ice assumed to be 1.9 km/s (Kohnen, 1974). The sediment layer is assumed to have a linear velocity gradient and is described by the three parameters of thickness, the shear velocity at the top discontinuity, and velocity gradient. Despite the fact that ice and sediment layers may have seismic anisotropy, we lack sufficient resolution in this study to resolve anisotropy at very shallow depths and thus parameterize these layers as isotropic. The lack of anisotropy resolution at very shallow depths results from Rayleigh wave group and phase velocity sensitivity kernels being sensitive to deeper depths than the Love wave kernels at the same period (Figure 1). With the shortest period of 8 s for both our Rayleigh and Love group and phase velocities estimates, the Rayleigh waves thus provide only poor constraints on the V_{SV} structure in the upper \sim 4 km. We tested the inversion by parameterizing the sediment layer as radially anisotropic for all nodes where the thickness of sediment was larger than 2 km and found that the result shows no constraints on anisotropy in sediment.

The mantle and crust are parameterized as radially anisotropic, as described by the Voigt average shear velocity and percentage of radial anisotropy. The velocity in the crust is described by eight parameters that characterize four-term B-splines describing the depth dependence of shear wave velocity and anisotropy, respectively. The mantle parameterization is similar to the crust but using six-term B-splines describing the depth dependence of velocity and anisotropy. However, limited by the period coverage and depth sensitivity of Love waves, we only perturb the top three B-splines, which constrain the shallow mantle. To stabilize the deep velocity structure, we smoothly connect the result with the ak135 model (Kennett et al., 1995) from 200 to 300 km. Overall, there are 18 free parameters in the inversion.

ZHOU ET AL. 9 of 23



The extensive ice shelves of Antarctica pose a complication to the normal three or four (with ice or water) layer parameterization used elsewhere. In these locations, up to several hundred meters of water layer may exist between the ice shelf and the sediment on the seafloor. The ice and water layers influence the Rayleigh wave velocities, whereas the Love wave eigenfunctions do not extend into the water and ice layers, so these layers have no effect on Love wave velocities. To invert the Love and Rayleigh waves simultaneously in this situation requires that each forward calculation of the dispersion curve from a velocity structure first calculate Rayleigh wave velocities based on the complete structure, followed by a calculation of the Love wave dispersion curves with the shelf region ice and water layers removed.

To ensure that every model is realistic, we include constraints based on prior information. Specifically, for the sediment-crust and crust-mantle boundary, the shear wave velocity must increase with depth, and the velocity gradient must be positive in the sediment layer since sediment compaction increases velocity. V_{SH} must be smaller than 5.1 km/s, and V_{SV} must be smaller than 4.9 km/s at all depths. Within the crust, we require that V_{SH} be smaller than 4.3 km/s and V_{SV} be smaller than 4.2 km/s based on the maximum velocities of crustal rocks (Christensen & Mooney, 1995; Christensen, 1996).

Random models for Monte Carlo sampling are generated from the prior distribution, which is based on perturbations around a starting model. The thickness of the sediment layer has an initial value of 4 km, with a perturbation range of 0–8 km. The Voigt average velocity in the crust and mantle is preset to the S_V velocity of an earlier joint inversion of Antarctic Rayleigh waves and receiver functions (Shen, Wiens, Anandakrishnan, et al., 2018). Both the Voigt average velocity and radial anisotropy are allowed to be perturbed up to $\pm 15\%$. The starting value for Moho depth is also taken from Shen, Wiens, Anandakrishnan, et al. (2018), and is allowed to vary up to ± 12 km.

4.2. Anisotropic Bayesian Monte Carlo Inversion

To obtain the shear wave velocity and anisotropy structure, we performed a Monte Carlo inversion of the Rayleigh and Love wave dispersion curves with the parameterization described above using the method of Shen, Ritzwoller, and Schulte-Pelkum (2013). For the forward models, we calculate dispersion curves for a transversely isotropic medium using the method of Herrmann, 2013. Note that this method calculates the true dispersion curves for anisotropic media rather than the approximate method of calculating Rayleigh and Love velocities from different isotropic models. A disadvantage of this method is that the forward calculation is 20 times slower than the isotropic calculation, which makes anisotropic inversion computationally expensive. The final inversion was finished on a high-performance computer cluster system and consumed about 1 million CPU hours.

For each grid point, the final resulting model is a set of 1-D structures representing the posterior parameter distributions, which were selected by Monte Carlo random walk based on the misfit to the observed data. The mean and standard deviation of the posterior model parameters are used to represent the 1-D structure and uncertainty of each grid point. Figure 6 shows an example of the inversion result at a grid point. Finally, the 3-D structure was constructed by combining the 1-D profile results on a 0.5° by 0.5° grid.

We ran sensitivity tests to examine the ability of the inversion to recover the various parameters, including sediment thickness, crustal structure, and anisotropy. We create a set synthetic structures based on a real inversion result from our model with different sediment thicknesses, and with all other parameters remaining the same (Figures S4–S7 in Supporting Information S1). Random noise based on the uncertainty at each period are added to the synthetic dispersion curve to simulate actual measurement error. With 3 km-thick sediment (Figure 7) in the input structure, the inversion is able to recover a similar structure within the uncertain range. The inversion is able to recover reasonable estimates of sediment thickness even in cases of 1–2 km-thick sediment. Further examples with different sediment thicknesses are shown in Supporting Information S1.

5. Results

5.1. Voigt Average Structure

The resulting Voigt average velocity structure (Figure 8) is similar in many respects to other recent shear wave models based on Rayleigh wave velocities from ambient noise correlation (O'Donnell et al., 2019; Shen, Wiens, Anandakrishnan, et al., 2018). The shallow structure is better resolved than previous studies, with very slow velocities observed in the Ross Embayment (RE), where thick sediments are found. Areas of low velocity

ZHOU ET AL. 10 of 23



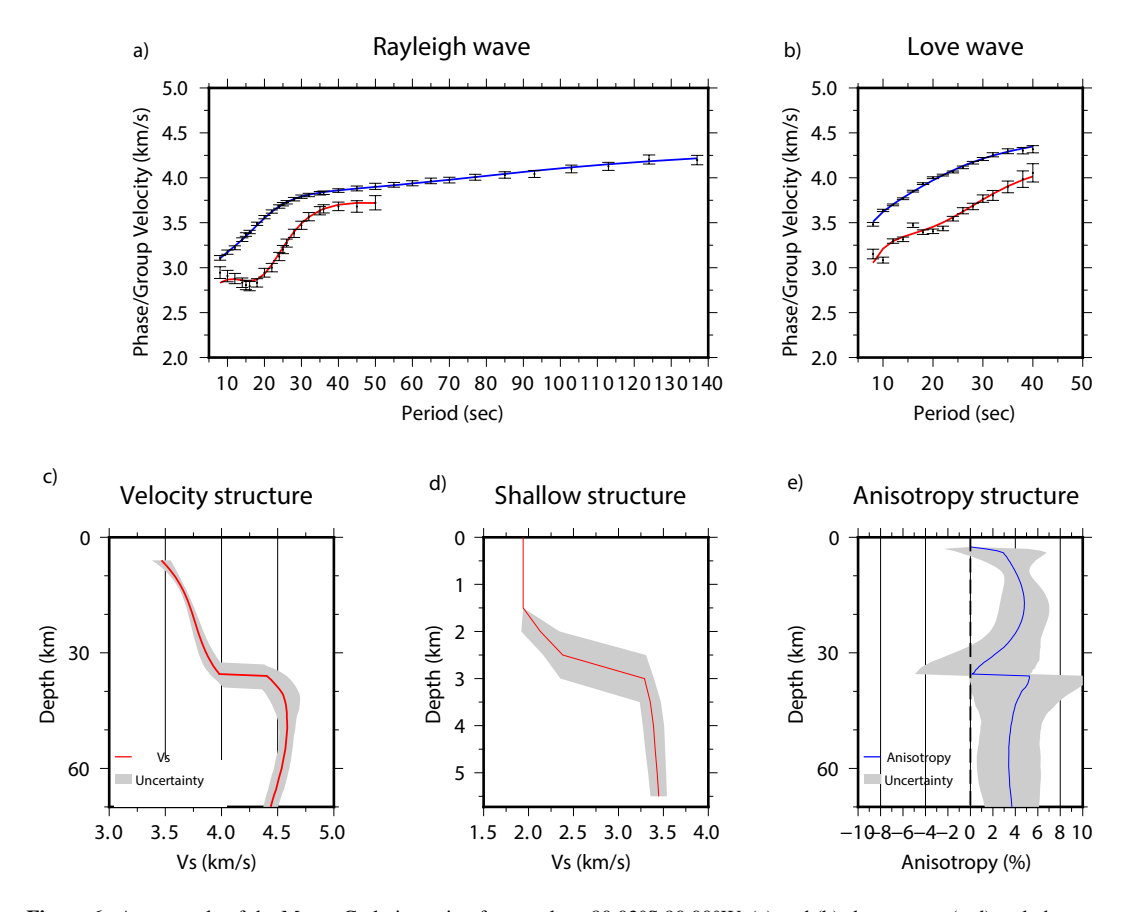


Figure 6. An example of the Monte Carlo inversion for a node at 80.03°S 90.00°W. (a) and (b) show group (red) and phase (blue) velocity fitting result for Rayleigh and Love waves respectively. The black points are observed data, and uncertainty is shown as the length of the bar. (c) and (d) shows the 1-D structure for this location. (c) shows the Voigt average shear wave velocity of the crust and mantle to 70 km, with the red line denoting the mean of the posterior distribution and the gray area representing the uncertainty range (one standard derivation). (d) shows the ice and sediment structure, legends are the same as the left figure. (e) shows the radial anisotropy structure. The blue line is the mean of the anisotropy posterior distribution. The gray area represents the uncertainty range.

 $(Vs \sim 3.6 \text{ km/s})$ are observed in the middle crust beneath prominent basins, such as the Bentley Trench and the Pensacola-Pole Basin. Low upper mantle velocities occur beneath the TAM and MBL. The derived crustal thickness is generally similar to that of Shen, Wiens, Anandakrishnan, et al. (2018), which was derived from Rayleigh wave dispersion and receiver functions and was used here as a starting model. Crustal thickness is also generally consistent with receiver function-constrained estimates at individual station sites (e.g., Chaput et al., 2014; Hansen et al., 2010). We observe the thickest crust (>55 km) in the GSM region. The TAM region shows a large crustal thickness gradient, with a much thinner crust (25–35 km) in WANT. The crustal thickness in the RE region is about 17–25 km, with a minimum thickness of 17 km. The uncertainty of crustal thickness in EANT is larger than WANT because the resolution kernels become broader for greater depths as well as the lower seismic station density.

5.2. Three-Dimensional Radial Anisotropy Structure

As shown in Figure 9, most areas of the upper crust show positive anisotropy ($V_{SH} > V_{SV}$), with amplitudes as high as 7%–8% in the Ross Embayment. There is some negative anisotropy beneath the South Pole region and the central and southern TAM. The middle and lower crust shows variable anisotropy, with regions of positive and negative values. The EM and parts of the WARS and RE show strong positive anisotropy, consistent with observations from other continents, which generally show positive anisotropy dominating the mid-to-lower crust (Moschetti et al., 2010b; Xie et al., 2013). Some well-resolved regions of negative anisotropy are also found, particularly at mid-to-lower crustal depths in the Pensacola-Pole Basin and throughout much of the WARS.

ZHOU ET AL. 11 of 23



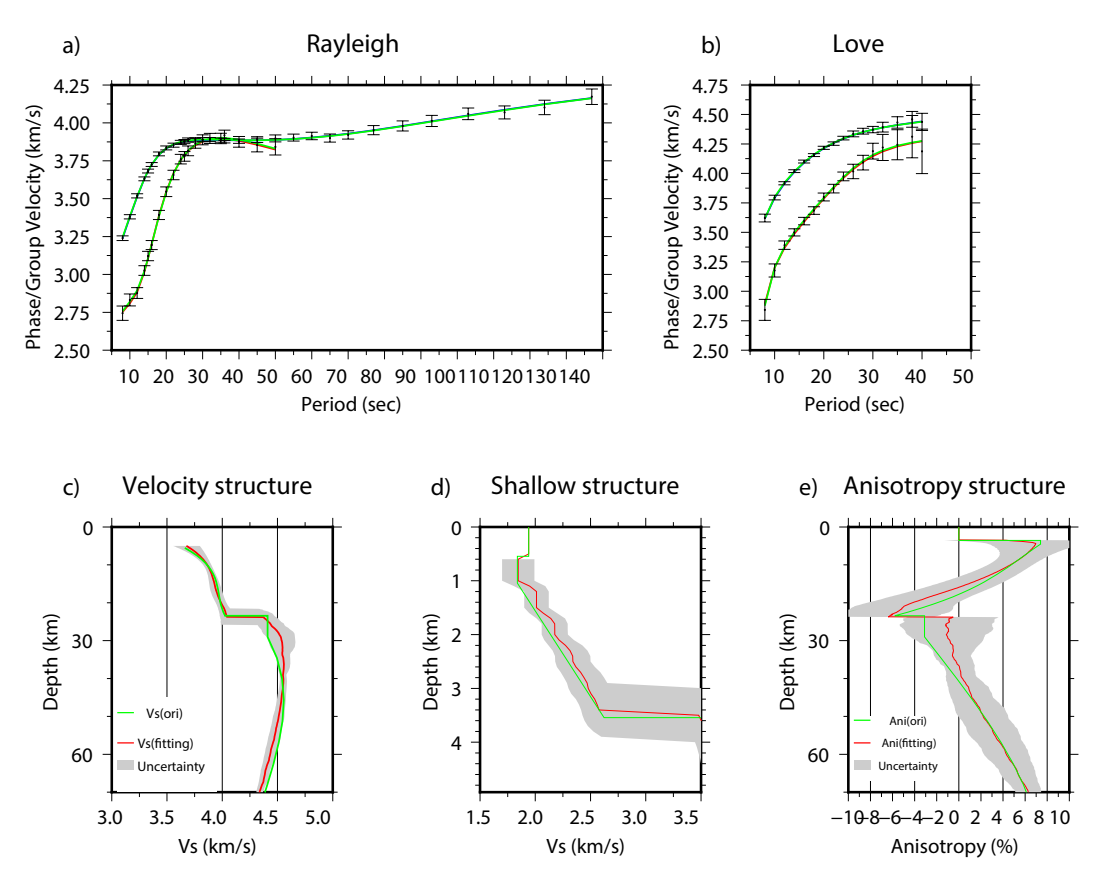


Figure 7. An example of the Monte Carlo inversion of synthetic data for a structure with 3 km thick sediment for a node in the Ross Embayment. (a) and (b) show group and phase velocity fitting results for Rayleigh and Love waves respectively. The green line is the predicted dispersion curve with no noise. The black points are synthetic data with noise added randomly within 1 standard deviation uncertainty, with the uncertainty shown as the length of the bar. The fitting curves are shown as blue (phase) and red (group) lines, which are almost identical to the green line. (c) and (d) shows the 1-D structure. (c) shows the Voigt average shear wave velocity of the crust and mantle to 70 km, with the red line denoting the mean of the posterior distribution and the gray area representing the uncertainty range (one standard derivation) and green line show the structure used to compute the synthetic data (d) shows the ice and sediment structure, and (e) shows the radial anisotropy structure. In each case the colored lines and gray area are as in panel c.

The uppermost mantle is characterized by positive anisotropy in most places. Relatively strong positive anisotropy (3%–8%) is found beneath the mountainous regions of the TAM, EM, and WM. The interior of EA shows weaker positive radial anisotropy (1%–5%) in most places. The predominance of positive radial anisotropy in the uppermost mantle is consistent with worldwide averages (Dziewonski & Anderson, 1981), as well as previous large-scale studies of Antarctica (Ritzwoller et al., 2001).

6. Discussion

6.1. Necessity of Radial Anisotropy

Since we invert the data using a radially anisotropic parameterization, which introduces additional model parameters, it is natural to ask whether these additional degrees of freedom are required, or if the parameterization is more complicated than required by the measured Love and Rayleigh wave velocity data. To investigate this, we attempted to fit the same datasets using a similar inversion, with the velocities constrained to be isotropic. Figure 10 shows an example of a comparison of isotropic and anisotropic inversion results for a location in West Antarctica. The results show that the fit for the isotropic model is extremely poor, with the residual norm increased by a factor of greater than two. The predicted Rayleigh wave phase velocities are too fast, and predicted Love wave phase velocities are too slow at many periods, as is expected when data from a structure with positive radial anisotropy is fit by an isotropic parameterization. The misfit is much larger than the estimated measurement

ZHOU ET AL. 12 of 23

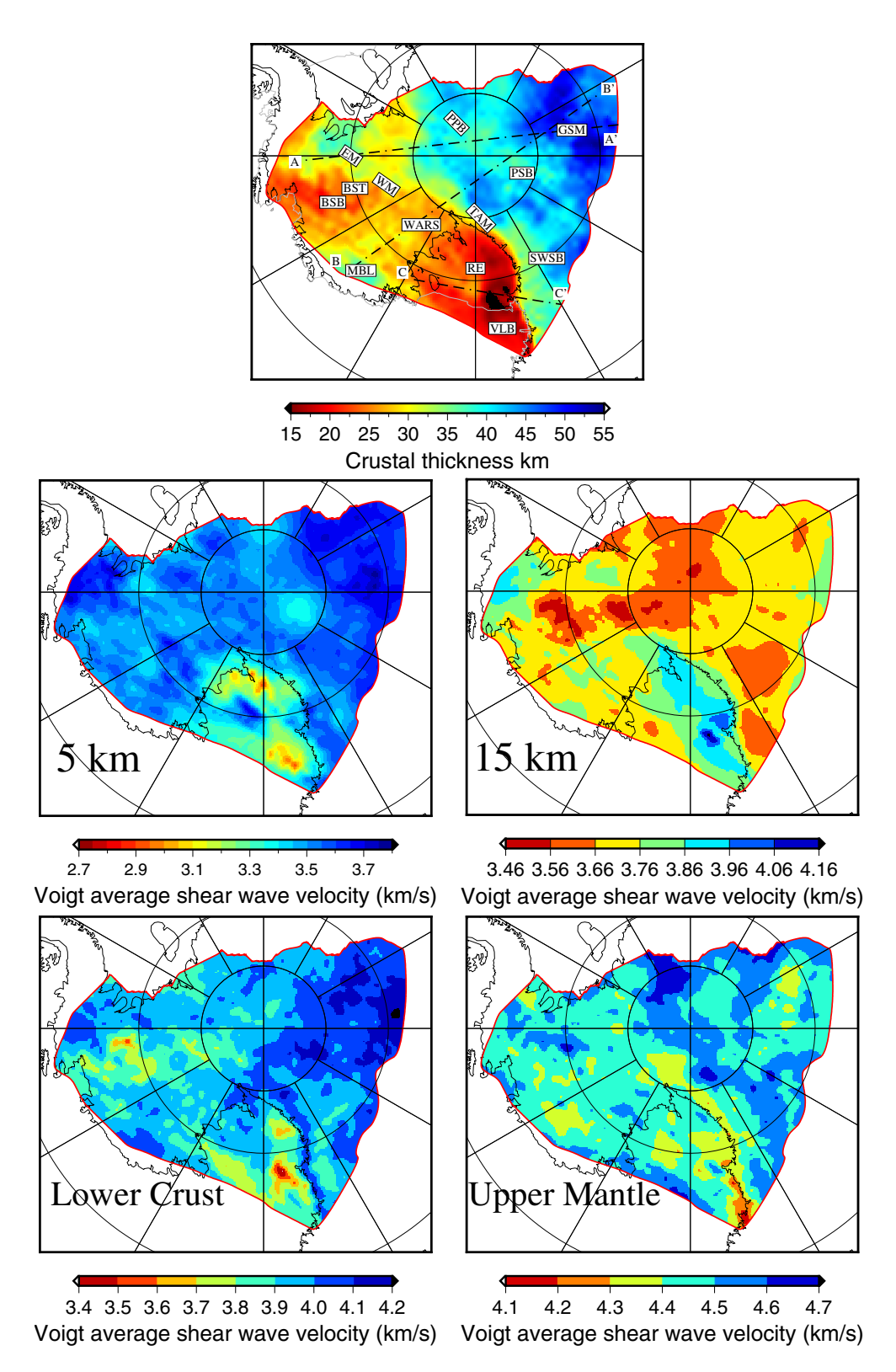


Figure 8. Top panel shows a map view of the crustal thickness of the study region along with the locations of profile lines (AA', BB', CC') in Figure 12. Abbreviations are the same as Figure 2. The lower two panels show Voigt average shear wave velocity at 5 km 15 km, 5 km above the Moho (lower crust) and the average between 5 and 15 km below Moho (upper mantle), respectively. The maps of uncertainty of the Voigt average shear wave velocity at same depth are shown at Figure S8 in Supporting Information S1.

ZHOU ET AL. 13 of 23



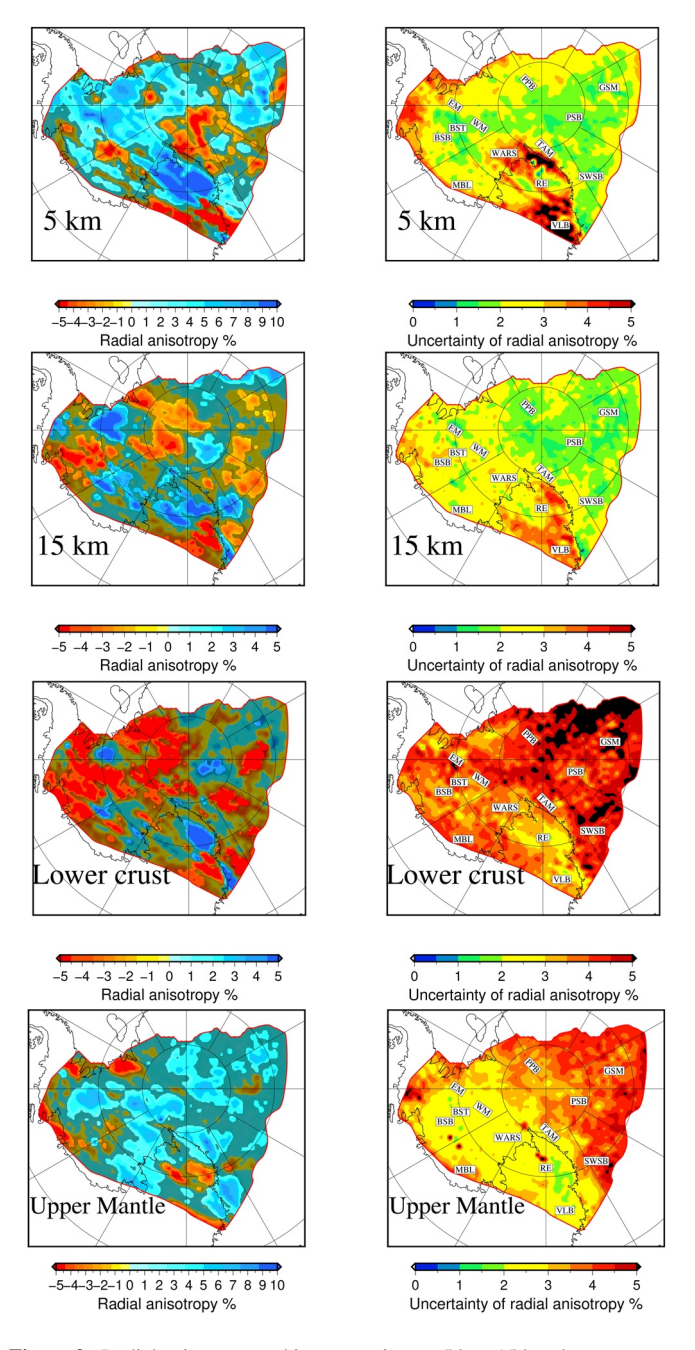


Figure 9. Radial anisotropy and its uncertainty at 5 km, 15 km, lower crust (5 km above Moho) and upper mantle (average between 5 and 15 km below Moho). For each depth, the left figure shows the radial anisotropy in percent. The area in which the anisotropy magnitude is larger than the standard deviation is shown in bright colors (as in the scale bar) and the regions with poorly determined anisotropy are shown with a darker mask using gray, light brown and dark brown. The right figures show the uncertainty (standard deviation) of the anisotropy. Abbreviations are the same as Figure 2.

uncertainty at many periods. In addition, we note that the Monte Carlo standard deviation of the anisotropy (Figure 10d) excludes the zero anisotropy case.

For most locations (95%), the anisotropic structure fits the data better, such that the isotropic model lies outside the standard deviation uncertainty bounds within some depth range. For 50% of the nodes, the anisotropic structure improves the misfit by 50%. For few locations (5%) where the anisotropy is poorly constrained, or only weak anisotropy is observed, both anisotropic and isotropic structures can fit the data within the standard deviation (Figure S3 in Supporting Information S1). In the sections below, only reliable anisotropy features where the anisotropy exceeds the Monte Carlo uncertainty bounds will be discussed and interpreted.

6.2. Sediment Thickness

The inclusion of Love wave data allows us to better constrain shallow crustal structure, including sediment thickness, compared to previous studies using Rayleigh wave data alone. The estimated sediment thickness is based on the thickness of shallow low-velocity material and will encompass unconsolidated sediments, sedimentary rocks, and weathered rocks of other types. Only a general estimate of sediment thickness is possible, as limited resolution requires the sediment velocities to be parameterized as a simple linear relationship with depth, as described above. Figure 11 shows the sediment thickness from the posterior result with uncertainties. The uncertainty of sediment thickness from the Monte-Carlo inversion is correlated with the absolute thickness and generally equal to 10%-40% of the determined sediment thickness in regions of thicker sediment, and 40%-80% of the sediment thickness in areas of thin sediment and at the edge of the model.

The inversion finds relatively thick sediment (\sim 4 \pm 1 km) in the Victoria Land Basin along the western margin of the Ross Embayment (RE), where seismic reflection and refraction studies have also identified basin sediment thicknesses as great as 8 km (ANTOSTRAT, 1995; Lindeque et al., 2016). Although the seismic results are highly smoothed and do not show smallscale details of the sediment distribution, the resolution of thick sediments with this well-known sedimentary basin lends confidence in the results. We find similar sediment thicknesses of around 4 km to the southeast, beneath the Ross Ice Shelf. Here sediments have been less well constrained by previous data, with some previous estimates based on gravity and magnetic models suggesting only 1–2 km of sediment in this region (Lindeque et al., 2016). However, preliminary results from the ROSETTA aerogeophysical project suggest sediments thicker than 3 km in this region estimated from the inferred depth to magnetic basement (Tankersley et al., 2021). Sediment thicknesses estimated in this study are more geographically smoothed, but are generally consistent with these recent ROSETTA results. The results from surface wave dispersion shown here indicate the existence of major sedimentary basins beneath the Ross Ice Shelf, with sediment thickness roughly equivalent to the basins north of the ice shelf margin.

The sediment thicknesses estimated for the rest of the study area show a complete absence of thick sedimentary cover (Figure 11). All of the interior

(subice) basins are characterized by total sediment thicknesses of less than 1.5 km and in most cases less than 1 km. For example, the South Pole Basin shows 0.8 ± 0.3 km sediment thickness, the Pensacola Pole Basin 1.0 ± 0.4 km, the Southern Wilkes Basin 1.0 ± 0.5 km, and the Byrd Basin and Bentley Trench 0.5 ± 0.2 km. In

ZHOU ET AL. 14 of 23

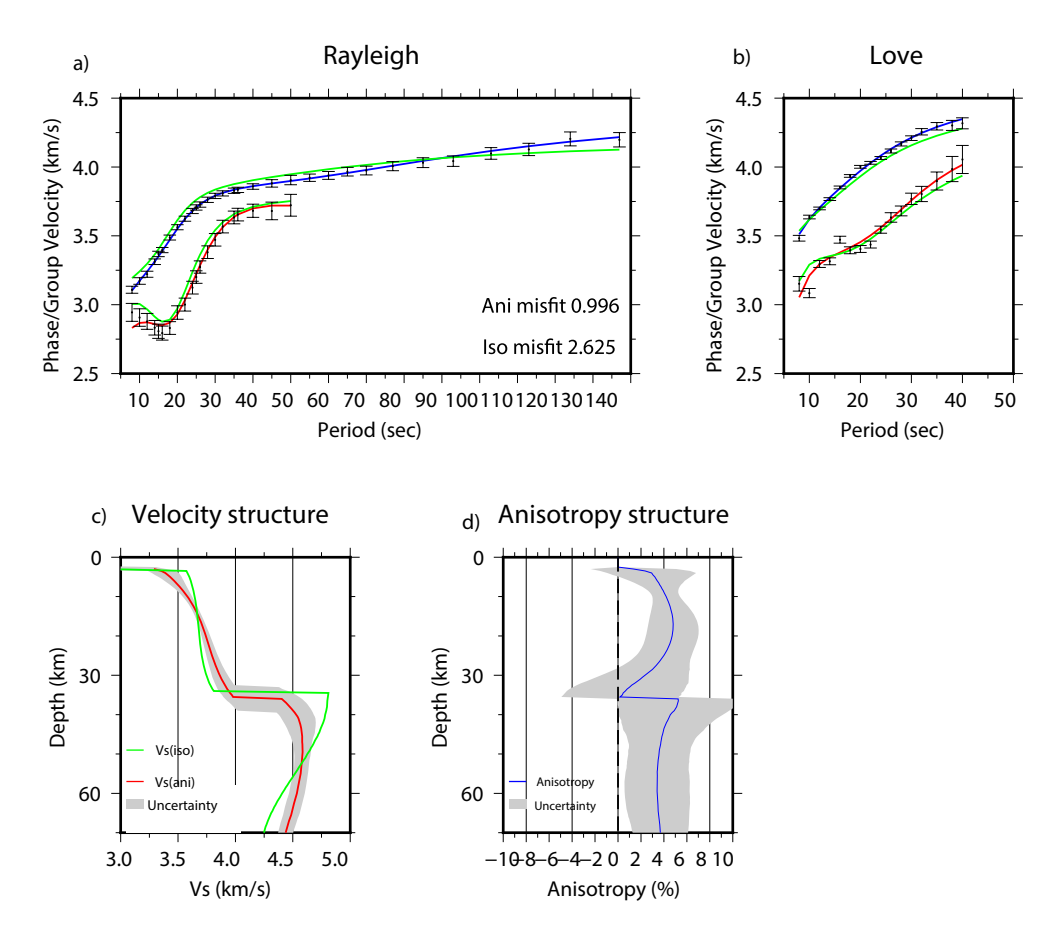


Figure 10. An example of the Monte Carlo inversion at 80.03°S 90.00°W (same as Figure 6) showing typical differences in fit between anisotropic and isotropic inversions. (a) and (b) show group (red) and phase (blue) velocity fitting result for Rayleigh and Love waves respectively. The black points are observed data, and uncertainty is shown as the length of the bar. Blue and red lines are fitting results for phase and group velocity respectively from the anisotropic inversion. The green lines are fitting results from the isotropic inversion. (c) shows the Voigt average shear wave velocity, the red line is the mean of the posterior distribution from the anisotropic inversion, the gray area represents uncertainty range (one standard derivation), the green line shows the shear wave velocity from the isotropic inversion. (d) shows the radial anisotropy structure. The blue line is the mean anisotropy of the posterior distribution. The gray area represents the uncertainty range.

West Antarctica (WA), even the basins that are closer to the coast do not show evidence for thick sediments, as demonstrated by the Thwaites glacier bed, which also shows less than 1 km of sediment.

These results are generally in accord with what little has been known prior to our study about sediment in these basins. Frederick et al. (2016) used aerogeophysical data to estimate an average sediment thickness of the Southern Wilkes Basin of \sim 1.6 km, but the region imaged in this study is farther south than their area of thicker sediments. Pyle et al. (2010) used Rayleigh waves from ambient seismic noise to constrain the sediment thickness of the Southern Wilkes Basin to be less than 2 km. Paxman et al. (2019) estimated an average sediment thickness of 1.6 ± 0.7 km in the Pensacola-Pole Basin based on aerogeophysical magnetic and gravity data. Pourpoint et al. (2019) used Love and Rayleigh wave phase velocities, Rayleigh H/V ratios, and receiver functions to estimate sediment thicknesses of 0.5–1.5 km for Byrd Basin, 0.8–1.3 km for Bentley Trench, and 0.8–1.3 km for the base of Thwaites Glacier. Dunham et al. (2020) estimated sediment thicknesses ranging from 0.1 to 0.8 km for various locations around Thwaites Glacier, Byrd Basin, and the Bentley Trench.

None of the interior basins of West and Central Antarctica have inferred sediment thicknesses of greater than 1.5 km. This is markedly different from most other continental regions worldwide. For example, major interior basins of North America, including Michigan, Illinois, Williston, and West Texas Permian Basins, show sediment thicknesses of between 4 and 7 km (Howell & van der Pluijm, 1999; Mooney & Kaban, 2010). The absence of greater sediment thickness in Antarctic basins may be largely due to the long-term positioning of the continent

ZHOU ET AL. 15 of 23

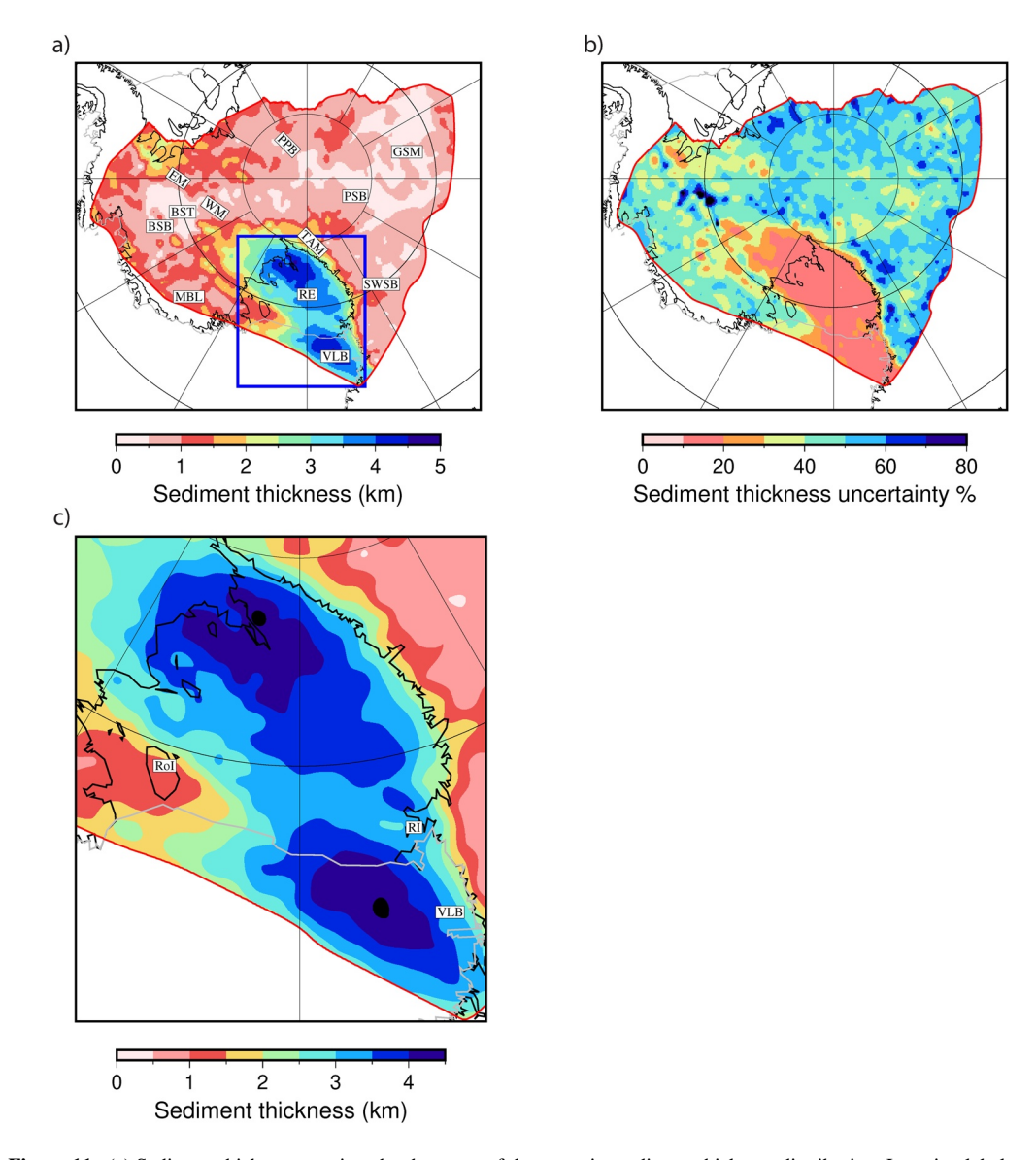


Figure 11. (a) Sediment thickness, as given by the mean of the posterior sediment thickness distribution. Location labels are the same as in Figure 2. The blue box shows the region in figure c. (b) the ratio of the sediment thickness uncertainty to the total sediment thickness, in percent. (c) Enlarged view of sediment thickness in the Ross Embayment region. Abbreviations: RoI - Roosevelt Island; RI – Ross Island.

at very high latitude. It is likely that long-term erosion rates have been very low on the interior of the Antarctic continent throughout the Phanerozoic (Cox et al., 2010), perhaps due to low precipitation rates and cold temperatures. This would have limited sediment supply and prevented the filling and isostatic deepening of interior basins. It is also possible that some significant prior sedimentary deposits have been glacially eroded along paths of glacial flow, such as suggested for the Pensacola-Pole basin (Paxman et al., 2019).

6.3. Radial Anisotropy of the Antarctic Crust

The anisotropic inversion shows strong positive radial anisotropy in the uppermost Antarctic continental crust (Figure 9), with the exception of a few smaller regions such as the Victoria Land Basin, Central TAM, and the Polar Subglacial Basin (PSB). This is in contrast to many other regions worldwide that show a predominance of negative anisotropy in the shallow crust (e.g., Movaghari et al., 2021; Xie et al., 2013). Negative radial and strong azimuthal anisotropy at shallow crustal depths is usually attributed to near-vertical cracks that remain open at

ZHOU ET AL. 16 of 23



shallow depths under low confining pressure (Crampin, 1994; Xie et al., 2013). One possible reason for the positive anisotropy of the uppermost crust in Antarctica is the larger confining pressure caused by large ice loads. The larger pressure will close the cracks in the shallow crust that typically control anisotropy at that depth. As a result, the radial anisotropy at shallow crustal depths in Antarctica may be controlled by the preferential orientation of anisotropic minerals such as mica, which often produce positive radial anisotropy in the crust (Lloyd et al., 2009).

The Ellsworth Mountains (EM) and the RE have large positive anisotropy in the crust, with the magnitude as large as 8% in the RE (Figures 8 and 11). The observation of positive radial anisotropy in the EM crust was reported by O'Donnell et al. (2019), but our results provide more details on both the depth-dependence and lateral distribution. In our imaging, the EM shows $5 \pm 2\%$ positive anisotropy throughout the crust, but the adjacent Whitmore Mountains (WM) only show strong positive radial anisotropy in the upper crust, and the middle to lower crust does not have a clear anisotropic pattern. Strong positive radial anisotropy in the middle to lower crust is broadly observed in other regions that have undergone extensional deformation, such as the North American Basin and Range, California, Tibet, Central North China, and Madagascar (Ai et al., 2020; Dreiling et al., 2018; Moschetti et al., 2010b; Wilgus et al., 2020; Xie et al., 2013). Positive crustal anisotropy is usually ascribed to highly anisotropic mica or amphibole minerals with a preferential orientation from horizontal compression or extension (Brownlee et al., 2017; Erdman et al., 2013; Lloyd et al., 2009). Our radial anisotropy result beneath EM and RE is consistent with the hypothesis that anisotropic minerals such as mica and amphiboles deformed under oriented stress can create positive radial anisotropy in the crust.

Large regions of strong negative anisotropy are found in the mid-to-lower crust beneath the Byrd Subglacial Basin (BSB) and Bentley Trench (BT) in central WA (Figures 9 and 12). Similar anisotropy is found on the other side of the WM just grid west of the South Pole near the Pensacola-Pole Basin (PPB). Both regions of strong negative anisotropy are also characterized by lower mid-to-lower crust shear velocities (Figure 8). Since these regions are thought to have moderate heat flow (e.g., Shen et al., 2020), the low velocities are unlikely to be of thermal origin and suggest a compositional variation that is correlated with the negative anisotropy. Negative anisotropy at mid-to lower crustal depths is less common than positive anisotropy in previous studies of other continental regions. When it has been observed, it has been attributed to mica sheets rotated to near-vertical orientations by vertical material transport or deformation (Xie et al., 2013), to preferred orientation of plagioclase under horizontal tectonic deformation (Wang et al., 2020), or to SPO from magma-filled near-vertical dikes in volcanic regions (Lynner et al., 2018).

The large regions of west and central Antarctica showing negative crustal anisotropy are not characterized by extensive active volcanism or extremely high heat flow, so the large extent of negative anisotropy cannot be due to magma-filled dikes. It is also unlikely that such a large region, with a geological history characterized by horizontal extension, has near-vertical foliation planes that would be required to produce negative anisotropy from minerals such as mica or amphibole. Recent studies show that plagioclase has extremely large seismic anisotropy, and develops LPO characterized by fast axes that are oriented perpendicular to the foliation plane (Bernard & Behr, 2017; Brownlee et al., 2017; Ji et al., 2014). Thus, crustal compositions with significant plagioclase and little mica and amphibole are expected to show negative anisotropy under horizontal extension. For example, Wang et al. (2020) interpret negative radial anisotropy pattern in the middle to lower crust beneath Southern California as due to plagioclase LPO. The correlation of negative anisotropy with lower velocities in the mid-to-lower crust suggests crustal composition variations may control the variation in radial anisotropy. The Vp/Vs ratio of 1.85 for plagioclase (Christensen & Mooney, 1995) results in lower shear velocities for rocks with high plagioclase content. In the absence of surface geological data and xenoliths from the region, we interpret the negative anisotropy and lower shear velocity in the mid- and lower crust as due to relatively felsic plagioclase-rich rocks that have been deformed by horizontal extension during rifting.

6.4. Radial Anisotropy of the Antarctic Uppermost Mantle

The Antarctic uppermost mantle shows mostly positive radial anisotropy (Figures 9 and 12), consistent with the average upper mantle worldwide (Dziewonski & Anderson, 1981). The predominance of positive radial anisotropy in the upper mantle is understood to result from the horizontal orientation of the fast direction of olivine anisotropy produced by LPO during deformation associated with plate motions and tectonic events (e.g., Becker et al., 2008). The strongest anisotropy occurs in the in the mountainous regions of the TAM, WM, and EM, where anisotropy values of up to 8% are observed. We interpret this distribution of strong positive radial anisotropy as

ZHOU ET AL. 17 of 23



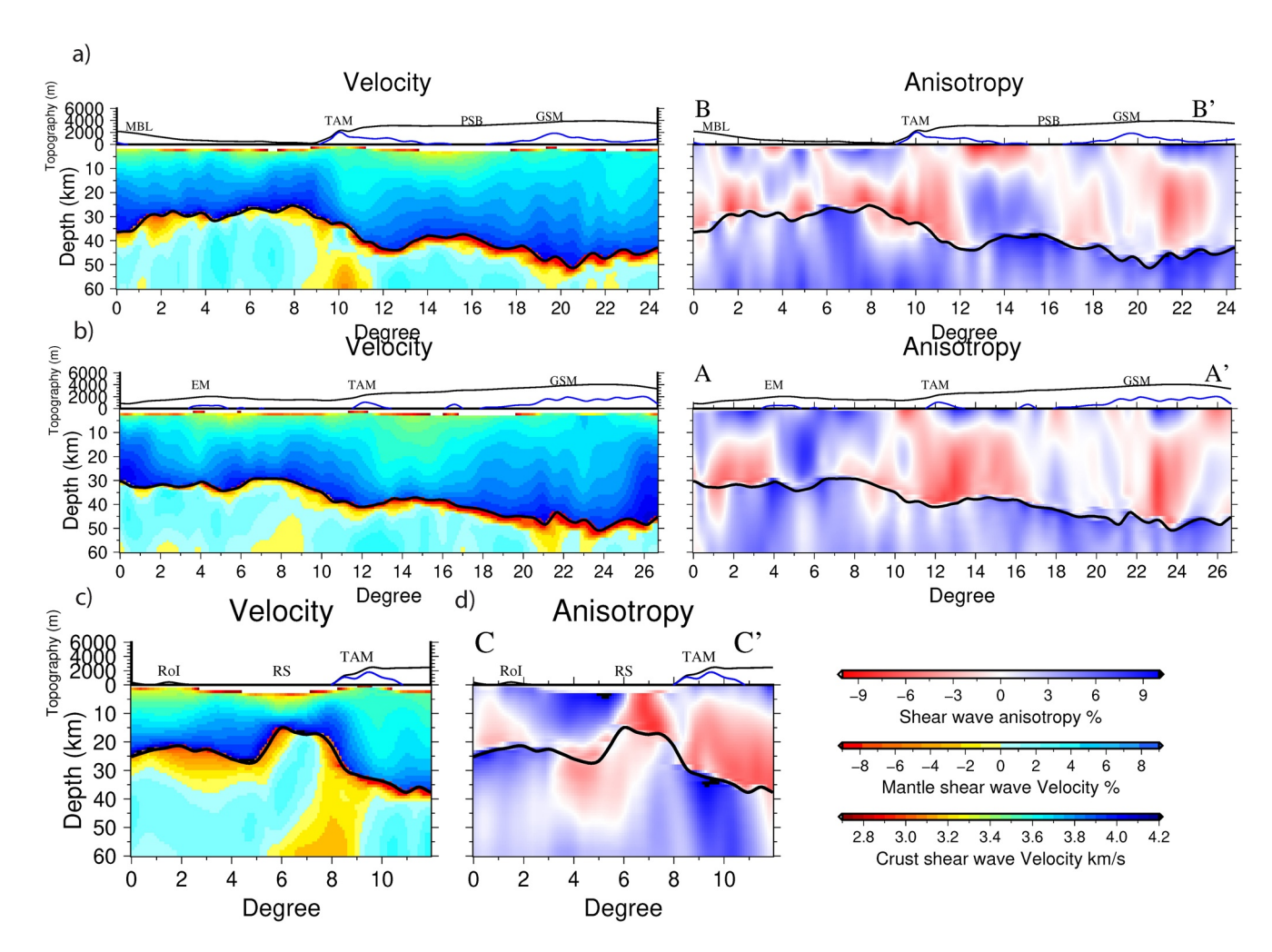


Figure 12. Three vertical profiles of 3D structure. The locations of the profiles are shown on the map in Figure 8 (top). For each profile (a, b, c), the left figure shows the Voigt average shear wave velocity from the surface to 60 km. The black lines on top shows the topography including ice, the blue lines show bedrock topography, and the red lines show the Moho. Crustal structure is shown as the shear velocity, and mantle structure is shown as velocity anomalies relative to the average velocity of 4.46 km/s (AA'), 4.48 km/s (BB') and 4.44 km/s (CC'), respectively. The right figure shows the radial anisotropy structure.

resulting from olivine LPO produced by Mesozoic and Cenozoic tectonic activity and associated mantle deformation. The areas of strong anisotropy along the TAM and WM correlate well with slow uppermost mantle velocities (Figure 8), consistent with significant asthenospheric flow in these areas.

Uppermost mantle radial anisotropy is stronger, on average, in WA and the TAM than in East Antarctica (Figure 9), consistent with the pattern of SKS splitting amplitudes for Antarctica (Accardo et al., 2014; Lucas, Accardo, et al., 2020). North America also shows stronger uppermost mantle radial anisotropy is found in regions of Phanerozoic tectonic activity with higher heat flow and lower seismic velocity compared to cratonic regions (Zhu et al., 2017). These observations suggest that areas of lower viscosity in the upper mantle and recent tectonic activity have stronger LPO and anisotropy compared to colder cratonic regions with little current deformation and anisotropy that is frozen in from past geological events.

The RE mantle shows an almost isotropic structure, except for a region near the volcanically active Ross Island that shows negative anisotropy. Mt Erebus on Ross Island and surrounding volcanoes have been suggested to be due to a mantle plume, formed by upwelling mantle material (e.g., Phillips et al., 2018). The negative anisotropy in this location may be due to LPO from vertical movement of mantle material associated with upwelling, or SPO from possible magma-filled near-vertical dikes.

ZHOU ET AL. 18 of 23



7. Conclusions

Based on broadband seismic data collected across the Antarctic continent from 2000 to 2018, we present a 3-D radially anisotropic model for the crust and uppermost mantle of West and Central Antarctica constrained by the group and phase speed of Rayleigh and Love waves derived from ambient noise cross-correlation. Utilizing nonlinear TF-pws stacking, we are able to get reliable phase and group velocity maps from 8 to 40 s for Love waves and 8–50 s for Rayleigh waves. We then invert these dispersion curves using a Baysian Monte-Carlo inversion to constrain shear velocity and radial anisotropy down to ~60 km.

Our result reveals several features of the crust and uppermost mantle structure, including (a) the sediment thickness of most sedimentary basins in the study area are less than 1.5 km, except for the Ross Embayment region, where sediment thicknesses of greater than 4 km were observed in the Victoria Land Basin and beneath the Ross Ice Shelf. (b) the shallow crust is characterized by strong positive anisotropy, which we attribute to LPO of micarich rocks, and may be enhanced by the increased pressure from the ice sheet that closes cracks and pore spaces. (c) The Ellsworth Mountains and Ross Embayment show strong positive anisotropy in the mid-to-lower crust, which is likely due to LPO of mica-rich rocks under horizontal extension. (d) Other regions of West and central Antarctica show strong negative anisotropy in the mid-to-lower crust, which we attribute to LPO of plagioclase under horizontal extension (e) Most of the uppermost mantle shows positive anisotropy, with strong anisotropy concentrated along the Transantarctic and Ellseworth Mountains, due to strong olivine LPO in regions of Phanerozoic tectonic activity. (f) West Antarctica shows somewhat stronger radial anisotropy than East Antarctica, due to the greater LPO in regions of recent tectonic activity relative to frozen-in anisotropy in the East Antarctic Craton. (g) In the Ross Embayment region, part of the uppermost mantle shows negative anisotropy, which we attribute to mantle flow or melt bodies associated with a mantle plume beneath the Ross Island and McMurdo volcanic province.

The 3-D shear wave velocity and radial anisotropy model we present can be used to better understand the deformation and flow pattern of the Antarctic continent. However, additional efforts can further improve both velocity and anisotropic structure. First, this 3-D anisotropic structure only resolves radial anisotropy, and further work is needed to constrain the broad pattern of azimuthal anisotropy in the crust and mantle. Second, due to limits of the station coverage and lower signal-to-noise ratio on horizontal components, as well as the difficulty in extracting Love wave velocities from earthquakes due to possible overtone contamination, no long period Love wave data were included in this study, restricting our understanding of the deeper anisotropic structure. As data and analysis techniques improve, combining both ambient and earthquake Rayleigh and Love wave data will no doubt further improve the resolution of deeper mantle structure. Third, to obtain better shallow structure constraints, particularly sediment thickness, introducing the estimation and inverse modeling of horizontal-to-vertical (*H/V*) amplitude ratios and high-frequency receiver functions jointly with Love and Rayleigh wave data will improve shallow resolution.

Acknowledgments

The authors would like to thank the support of all field teams who collected the data, especially Patrick Shore and Andrew J. Lloyd. This work is supported by the National Science Foundation under grants OPP-1744889 (Douglas A. Wien), OPP-1744852 (Douglas A. Wien), OPP-1945693 (Douglas A. Wien). OPP-1945856 (Weisen Shen) and EAR-1600087 (Weisen Shen). Seismic instruments and field support were provided by the Incorporated Research Institutions for Seismology (IRIS) through the PASSCAL Instrument Center at New Mexico Tech. Data collected will be available through the IRIS Data Management Center. The facilities of IRIS Data Management Center (https:// ds.iris.edu/ds/nodes/dmc/) were used for access data used in this study. IRIS Data Services are funded through the Seismological Facilities for the Advancement of Geoscience (SAGE) Award of the National Science Foundation under Cooperative Support Agreement EAR-1851048

Data Availability Statement

The phase weighted stacking software package is available at https://github.com/sergiventosa/ts-PWS (https://doi.org/10.5281/zenodo.1154587). Computer codes for the forward simulations are from Computer Programs in Seismology (Herrmann, 2013), and are available at http://www.eas.slu.edu/eqc/eqccps.html. Seismic data used in this study will be available through the IRIS Data Management Center (https://ds.iris.edu/ds/nodes/dmc/)

References

Accardo, N., Wiens, D., Hernandez, S., Aster, R., Nyblade, A., Huerta, A., et al. (2014). Upper mantle seismic anisotropy beneath the West Antarctic Rift System and surrounding region from shear wave splitting analysis. *Geophysical Journal International*, 198(1), 414–429. https://doi.org/10.1093/gji/ggu117

Ai, S., Zheng, Y., & Wang, S. (2020). Crustal deformations of the central North China craton constrained by radial anisotropy. Journal of Geophysical Research: Solid Earth, 125. https://doi.org/10.1029/2019jb018374

An, M., Wiens, D. A., Zhao, Y., Feng, M., Nyblade, A. A., Kanao, M., et al. (2015). S-velocity model and inferred Moho topography beneath the Antarctic Plate from Rayleigh waves. *Journal of Geophysical Research: Solid Earth, 120*(1), 359–383. https://doi.org/10.1002/2014JB011332

Anthony, R. E., Aster, R. C., Wiens, D., Nyblade, A., Anandakrishnan, S., Huerta, A., et al. (2015). The Seismic Noise Environment of Antarctica. *Seismological Research Letters*, 86(1), 89–100. https://doi.org/10.1785/0220140109

Antostrat (1995). Seismic stratigraphic atlas of the Ross Sea. Geology and Seismic Stratigraphy of the Antarctic Margin, 68.

ZHOU ET AL. 19 of 23



- Barberini, V., Burlini, L., & Zappone, A. (2007). Elastic properties, fabric and seismic anisotropy of amphibolites and their contribution to the lower crust reflectivity. *Tectonophysics*, 445(3–4), 227–244. https://doi.org/10.1016/j.tecto.2007.08.017
- Barklage, M., Wiens, D. A., Nyblade, A., & Anandakrishnan, S. (2009). Upper mantle seismic anisotropy of South Victoria Land and the Ross Sea coast, Antarctica from SKS and SKKS splitting analysis. *Geophysical Journal International*, 178(2), 729–741. https://doi.org/10.1111/j.1365-246x.2009.04158.x
- Barletta, V. R., Bevis, M., Smith, B. E., Wilson, T., Brown, A., Bordoni, A., et al. (2018). Observed rapid bedrock uplift in Amundsen Sea Embayment promotes ice-sheet stability. *Science*, 360(6395), 1335–1339. https://doi.org/10.1126/science.aao1447
- Barmin, M., Ritzwoller, M., & Levshin, A. (2001). A fast and reliable method for surface wave tomography. *Pure and Applied Geophysics*, 158(8), 1351–1375. https://doi.org/10.1007/pl00001225
- Becker, T. W., Kustowski, B., & Ekström, G. (2008). Radial seismic anisotropy as a constraint for upper mantle rheology. *Earth and Planetary Science Letters*, 267(1–2), 213–227. https://doi.org/10.1016/j.epsl.2007.11.038
- Bensen, G. D., Ritzwoller, M. H., Barmin, M. P., Levshin, A. L., Lin, F., Moschetti, M. P., et al. (2007). Processing seismic ambient noise data to obtain reliable broad-band surface wave dispersion measurements. *Geophysical Journal International*, 169(3), 1239–1260. https://doi.org/10.1111/j.1365-246X.2007.03374.x
- Bernard, R. E., & Behr, W. M. (2017). Fabric heterogeneity in the Mojave lower crust and lithospheric mantle in Southern California. *Journal of Geophysical Research: Solid Earth*, 122, 5000–5025. https://doi.org/10.1002/2017jb014280
- Bialas, R. W., Buck, R. W., Studinger, M., & Fitzgerald, P. G. (2007). Plateau collapse model for the Transantarctic Mountains—West Antarctic Rift System: Insights from numerical experiments. *Geology*, 35(8), 687–690. https://doi.org/10.1130/g23825a.1
- Bingham, R. G., Ferraccioli, F., King, E. C., Larter, R. D., Pritchard, H. D., Smith, A. M., & Vaughan, D. G. (2012). Inland thinning of West Antarctic Ice Sheet steered along subglacial rifts. *Nature*, 487(7408), 468–471. https://doi.org/10.1038/nature11292
- Boger, S. D. (2011). Antarctica Before and after Gondwana. Gondwana Research, 19(2), 335–371. https://doi.org/10.1016/j.gr.2010.09.003
 Brocher, T. M. (2005). Empirical relations between elastic wavespeeds and density in the Earth's Crust. Bulletin of the Seismological Society of America, 95(6), 2081–2092. https://doi.org/10.1785/0120050077
- Bromirski, P. D., Diez, A., Gerstoft, P., Stephen, R. A., Bolmer, T., Wiens, D. A., et al. (2015). Ross Ice Shelf vibrations. *Geophysical Research Letters*, 42(18), 7589–7597. https://doi.org/10.1002/2015gl065284
- Brownlee, S. J., Schulte-Pelkum, V., Raju, A., Mahan, K., Condit, C., & Orlandini, O. F. (2017). Characteristics of deep crustal seismic anisotropy from a compilation of rock elasticity tensors and their expression in receiver functions. *Tectonics*, 36(9), 1835–1857. https://doi.org/10.1002/2017tc004625
- Chaput, J., Aster, R., Huerta, A., Sun, X., Lloyd, A., Wiens, D., et al. (2014). The crustal thickness of West Antarctica. *Journal of Geophysical Research: Solid Earth*, 119, 378–395. https://doi.org/10.1002/2013JB010642
- Christensen, N. I. (1996). Poisson's ratio and crustal seismology. Journal of Geophysical Research, 101(B2), 3139–3156. https://doi. org/10.1029/95ib03446
- Christensen, N. I., & Mooney, W. D. (1995). Seismic velocity structure and composition of the continental crust: A global view. *Journal of Geophysical Research*, 100(B6), 9761–9788. https://doi.org/10.1029/95jb00259
- Cox, S. E., Thomson, S. N., Reiners, P. W., Hemming, S. R., & Flierdt, T. (2010). Extremely low long-term erosion rates around the Gamburtsev Mountains in interior East Antarctica. *Geophysical Research Letters*, 37(22). https://doi.org/10.1029/2010gl045106
- Crampin, S. (1994). The fracture criticality of crustal rocks. Geophysical Journal International, 118(2), 428–438. https://doi.org/10.1111/j.1365-246x.1994.tb03974.x
- Dalton, C. A., & Gaherty, J. B. (2013). Seismic anisotropy in the continental crust of northwestern Canada. *Geophysical Journal International*, 193(1), 338–348. https://doi.org/10.1093/gjj/ggs108
- Dreiling, J., Tilmann, F., Yuan, X., Giese, J., Rindraharisaona, E. J., Rümpker, G., & Wysession, M. E. (2018). Crustal radial anisotropy and linkage to geodynamic processes: A study based on seismic ambient noise in Southern Madagascar. *Journal of Geophysical Research: Solid Earth*, 123, 5130–5146. https://doi.org/10.1029/2017JB015273
- Dunham, C. K., O'Donnell, J. P., Stuart, G. W., Brisbourne, A. M., Rost, S., Jordan, T. A., et al. (2020). A joint inversion of receiver function and Rayleigh wave phase velocity dispersion data to estimate crustal structure in West Antarctica. *Geophysical Journal International*, 223, 1644–1657. https://doi.org/10.1093/gii/geaa398
- Dziewonski, A., Bloch, S., & Landisman, M. (1969). A technique for the analysis of transient seismic signals. *Bulletin of the Seismological Society of America*, 59, 427–444. https://doi.org/10.1785/bssa0590010427
- Dziewonski, A. M., & Anderson, D. L. (1981). Preliminary reference Earth model. *Physics of the Earth and Planetary Interiors*, 25(4), 297–356. https://doi.org/10.1016/0031-9201(81)90046-7
- Emry, E. L., Nyblade, A. A., Julià, J., Anandakrishnan, S., Aster, R. C., Wiens, D. A., et al. (2015). The mantle transition zone beneath West Antarctica: Seismic evidence for hydration and thermal upwellings. Geochemistry, Geophysics, Geosystems, 16(1), 40–58. https://doi. org/10.1002/2014gc005588
- Erdman, M. E., Hacker, B. R., Zandt, G., & Seward, G. (2013). Seismic anisotropy of the crust: Electron-backscatter diffraction measurements from the Basin and Range. *Geophysical Journal International*, 195(2), 1211–1229. https://doi.org/10.1093/gji/ggt287
- Feng, L., & Ritzwoller, M. H. (2019). A 3-D shear velocity model of the crust and uppermost mantle beneath Alaska including apparent radial anisotropy. *Journal of Geophysical Research: Solid Earth*, 124, 10468–10497. https://doi.org/10.1029/2019jb018122
- Ferraccioli, F., Finn, C. A., Jordan, T. A., Bell, R. E., Anderson, L. M., & Damaske, D. (2011). East Antarctic rifting triggers uplift of the Gamburtsev Mountains. Nature, 479(7373), 1056–6392. https://doi.org/10.1038/nature10566
- Ferreira, A. M. G., Faccenda, M., Sturgeon, W., Chang, S.-J., & Schardong, L. (2019). Ubiquitous lower-mantle anisotropy beneath subduction zones. *Nature Geoscience*, 12(4), 301–306. https://doi.org/10.1038/s41561-019-0325-7
- Finotello, M., Nyblade, A., Julia, J., Wiens, D., & Anandakrishnan, S. (2011). Crustal Vp–Vs ratios and thickness for Ross Island and the Transant-arctic Mountain front, Antarctica. *Geophysical Journal International*, 185(1), 85–92. https://doi.org/10.1111/j.1365-246x.2011.04946.x
- Fitzgerald, P. G. (2002). Tectonics and landscape evolution of the Antarctic plate since the breakup of Gondwana, with an emphasis on the West Antarctic Rift System and the Transantarctic Mountains. In J. Gamble, D. Skinner, & S. Henrys (Eds.) (Vol. 35, pp. 453–469). Wellington, New Zealand: The Royal Society of New Zealand.
- Flierdt, T., Hemming, S. R., Goldstein, S. L., Gehrels, G. E., & Cox, S. E. (2008). Evidence against a young volcanic origin of the Gamburtsev Subglacial Mountains, Antarctica. *Geophysical Research Letters*, 35. https://doi.org/10.1029/2008gl035564
- Frederick, B. C., Young, D. A., Blankenship, D. D., Richter, T. G., Kempf, S. D., Ferraccioli, F., & Siegert, M. J. (2016). Distribution of subglacial sediments across the Wilkes Subglacial Basin, East Antarctica. *Journal of Geophysical Research: Earth Surface*, 121(4), 790–813. https://doi.org/10.1002/2015jf003760

ZHOU ET AL. 20 of 23



- Fretwell, P., Pritchard, H. D., Vaughan, D. G., Bamber, J. L., Barrand, N. E., Bell, R., et al. (2012). Bedmap2: Improved ice bed, surface and thickness datasets for Antarctica. *The Cryosphere Discussions*, 6(5), 4305–4361. https://doi.org/10.5194/tcd-6-4305-2012
- Goodge, J. W., Fanning, C. M., & Bennett, V. C. (2001). U–Pb evidence of ~1.7 Ga crustal tectonism during the Nimrod Orogeny in the Transantarctic Mountains, Antarctica: Implications for Proterozoic plate reconstructions. *Precambrian Research*, 112(3–4), 261–288. https://doi.org/10.1016/s0301-9268(01)00193-0
- Granot, R., & Dyment, J. (2018). Late Cenozoic unification of East and West Antarctica. *Nature Communications*, 9(1). https://doi.org/10.1038/s41467-018-05270-w
- Graw, J. H., Adams, A. N., Hansen, S. E., Wiens, D. A., Hackworth, L., & Park, Y. (2016). Upper mantle shear wave velocity structure beneath northern Victoria Land, Antarctica: Volcanism and uplift in the northern Transantarctic Mountains. *Earth and Planetary Science Letters*, 449, 48–60. https://doi.org/10.1016/j.epsl.2016.05.026
- Graw, J. H., & Hansen, S. E. (2017). Upper mantle seismic anisotropy beneath the Northern Transantarctic Mountains, Antarctica from PKS, SKS, and SKKS splitting analysis: Anisotropy beneath the Northern tams. Geochemistry, Geophysics, Geosystems, 18(2), 544–557. https://doi.org/10.1002/2016gc006729
- Guo, Z., Gao, X., Wang, W., & Yao, Z. (2012). Upper- and mid-crustal radial anisotropy beneath the central Himalaya and southern Tibet from seismic ambient noise tomography. Geophysical Journal International, 189(2), 1169–1182. https://doi.org/10.1111/j.1365-246X.2012.05425.x
- Guo, Z., Yang, Y., & Chen, Y. J. (2016). Crustal radial anisotropy in Northeast China and its implications for the regional tectonic extension. Geophysical Journal International, 207(1), 197–208. https://doi.org/10.1093/gji/ggw261
- Hansen, P. (1999). The L-curve and its use in the numerical treatment of inverse problems.
- Hansen, S. E., Graw, J. H., Kenyon, L. M., Nyblade, A. A., Wiens, D. A., Aster, R. C., et al. (2014). Imaging the Antarctic mantle using adaptively parameterized P-wave tomography: Evidence for heterogeneous structure beneath West Antarctica. Earth and Planetary Science Letters, 408, 66–78. https://doi.org/10.1016/j.epsl.2014.09.043
- Hansen, S. E., Nyblade, A. A., Heeszel, D. S., Wiens, D. A., Shore, P., & Kanao, M. (2010). Crustal structure of the Gamburtsev Mountains, East Antarctica, from S-wave receiver functions and Rayleigh wave phase velocities. Earth and Planetary Science Letters, 300(3-4), 395-401. https://doi.org/10.1016/j.epsl.2010.10.022
- Hansen, S. E., Reusch, A. M., Parker, T., Bloomquist, D. K., Carpenter, P., Graw, J. H., & Brenn, G. R. (2015). The Transantarctic Mountains Northern Network (TAMNNET): Deployment and Performance of a Seismic Array in Antarctica. Seismological Research Letters, 86(6), 1636–1644. https://doi.org/10.1785/0220150117
- Heeszel, D. S., Wiens, D. A., Anandakrishnan, S., Aster, R. C., Dalziel, I. W., Huerta, A. D., et al. (2016). Upper mantle structure of central and West Antarctica from array analysis of Rayleigh wave phase velocities. *Journal of Geophysical Research*, 121, 1758–1775. https://doi.org/10.1002/2015JB012616
- Heeszel, D. S., Wiens, D. A., Nyblade, A. A., Hansen, S. E., Kanao, M., An, M., & Zhao, Y. (2013). Rayleigh wave constraints on the structure and tectonic history of the Gamburtsev Subglacial Mountains, East Antarctica. *Journal of Geophysical Research: Solid Earth*, 118, 2138– 2153. https://doi.org/10.1002/jgrb.50171
- Herrmann, R. B. (2013). Computer programs in seismology: An evolving tool for instruction and research. Seismological Research Letters, 84(6), 1081–1088. https://doi.org/10.1785/0220110096
- Howell, P. D., & van der Pluijm, B. A. (1999). Structural sequences and styles of subsidence in the Michigan basin. GSA Bull, 111, 974–991. https://doi.org/10.1130/0016-7606(1999)111<0974:SSASOS>2.3.CO;2
- Huerta, A. D., & Harry, D. L. (2007). The transition from diffuse to focused extension: Modeled evolution of the West Antarctic Rift system. Earth and Planetary Science Letters, 255(1–2), 133–147. https://doi.org/10.1016/j.epsl.2006.12.011
- Illsley-Kemp, F., Savage, M. K., Wilson, C. J. N., & Bannister, S. (2019). Mapping stress and structure from subducting slab to magmatic rift: Crustal seismic anisotropy of the North Island, New Zealand. Geochemistry, Geophysics, Geosystems, 20(11), 5038–5056. https://doi. org/10.1029/2019gc008529
- Ji, S., Shao, T., Salisbury, M. H., Sun, S., Michibayashi, K., Zhao, W., et al. (2014). Plagioclase preferred orientation and induced seismic anisotropy in mafic igneous rocks. *Journal of Geophysical Research: Solid Earth*, 119, 8064–8088. https://doi.org/10.1002/2014JB011352
- Jordan, T. A., Ferraccioli, F., & Leat, P. T. (2017). New geophysical compilations link crustal block motion to Jurassic extension and strike-slip faulting in the Weddell Sea Rift System of West Antarctica. Gondwana Research, 42, 29–48. https://doi.org/10.1016/j.gr.2016.09.009
- Jordan, T. A., Ferraccioli, F., Vaughan, D. G., Holt, J. W., Corr, H., Blankenship, D. D., & Diehl, T. M. (2010). Aerogravity evidence for major crustal thinning under the Pine Island Glacier region (West Antarctica). GSA Bulletin, 122(5–6), 714–726. https://doi.org/10.1130/b26417.1
- Jordan, T. A., Riley, T. R., & Siddoway, C. S. (2020). The geological history and evolution of West Antarctica. Nature Reviews Earth & Environment, 1(2), 117–133. https://doi.org/10.1038/s43017-019-0013-6
- Kanasewich, E., Alpaslan, T., & Hemmings, C. (1973). Nth-root stack nonlinear multichannel filter. Geophysics, 38(2), 327–338. https://doi.org/10.1190/1.1440343
- Karato, S., Jung, H., Katayama, I., & Skemer, P. (2008). Geodynamic significance of seismic anisotropy of the upper mantle: New insights from laboratory studies. *Annual Review of Earth and Planetary Sciences*, 36(1), 59–95. https://doi.org/10.1146/annurev.earth.36.031207.124120
- Kennett, B. L. N., Engdahl, E. R., & Buland, R. (1995). Constraints on seismic velocities in the Earth from traveltimes. Geophysical Journal International, 122(1), 108–124. https://doi.org/10.1111/j.1365-246x.1995.tb03540.x
- Kohnen, H. (1974). The temperature dependence of seismic waves in ice. *Journal of Glaciology*, 13(67), 144–147. https://doi.org/10.3189/s0022143000023467
- Lawrence, J. F., Wiens, D. A., Nyblade, A. A., Anandakrishnan, S., Shore, P. J., & Voigt, D. (2006a). Crust and upper mantle structure of the Transantarctic Mountains and surrounding regions from receiver functions, surface waves, and gravity: Implications for uplift models. Geochemistry, Geophysics, Geosystems, 7, Q10011. https://doi.org/10.1029/2006GC001282
- Lawrence, J. F., Wiens, D. A., Nyblade, A. A., Anandakrishnan, S., Shore, P. J., & Voigt, D. (2006b). Rayleigh wave phase velocity analysis of the Ross Sea, transantarctic mountains and east Antarctica from a temporary seismograph array. *Journal of Geophysical Research*, 111, B06302. https://doi.org/10.1029/2005jb003812
- Lawrence, J. F., Wiens, D. A., Nyblade, A. A., Anandakrishan, S., Shore, P. J., & Voigt, D. (2006c). Upper mantle thermal variations beneath the Transantarctic Mountains inferred from teleseismic S-wave attenuation. *Geophysical Research Letters*, 33. https://doi.org/10.1029/2005gl024516
- LeMasurier, W. E. (1990). Late Cenozoic volcanism on the Antarctic Plate: An overview (pp. 1–17). American Geophysical Union. https://doi.org/10.1029/ar048p0001
- Li, G., Niu, F., Yang, Y., & Xie, J. (2018). An investigation of time-frequency domain phase-weighted stacking and its application to phase-velocity extraction from ambient noise's empirical Green's functions. *Geophysical Journal International*, 212(2), 1143–1156. https://doi.org/10.1093/gji/ggx448

ZHOU ET AL. 21 of 23



- Lin, F., Moschetti, M. P., & Ritzwoller, M. H. (2008). Surface wave tomography of the western United States from ambient seismic noise: Rayleigh and Love wave phase velocity maps. *Geophysical Journal International*, 173(1), 281–298. https://doi.org/10.1111/j.1365-246x.2008.03720.x
- Lin, F., Ritzwoller, M. H., Townend, J., Bannister, S., & Savage, M. K. (2007). Ambient noise Rayleigh wave tomography of New Zealand. Geophysical Journal International, 170(2), 649–666. https://doi.org/10.1111/j.1365-246x.2007.03414.x
- Lindeque, A., Gohl, K., Wobbe, F., & Uenzelmann-Neben, G. (2016). Preglacial to glacial sediment thickness grids for the Southern Pacific Margin of West Antarctica. Geochemistry, Geophysics, Geosystems, 17(10), 4276–4285. https://doi.org/10.1002/2016GC006401
- Lloyd, A. J., Nyblade, A. A., Wiens, D. A., Hansen, S. E., Kanao, M., Shore, P. J., & Zhao, D. (2013). Upper mantle seismic structure beneath central East Antarctica from body wave tomography: Implications for the origin of the Gamburtsev Subglacial Mountains. Geochemistry, Geophysics, Geosystems, 14(4), 902–920. https://doi.org/10.1002/ggge.20098
- Lloyd, A. J., Wiens, D. A., Nyblade, A. A., Anandakrishnan, S., Aster, R. C., Huerta, A. D., et al. (2015). A seismic transect across West Antarctica: Evidence for mantle thermal anomalies beneath the Bentley Subglacial Trench and the Marie Byrd Land Dome. *Journal of Geophysical Research: Solid Earth*, 120, 8439–8460. https://doi.org/10.1002/2015jb012455
- Lloyd, G. E., Butler, R. W. H., Casey, M., & Mainprice, D. (2009). Mica, deformation fabrics and the seismic properties of the continental crust. Earth and Planetary Science Letters, 288(1–2), 320–328. https://doi.org/10.1016/j.epsl.2009.09.035
- Long, M. D., & Becker, T. W. (2010). Mantle dynamics and seismic anisotropy. Earth and Planetary Science Letters, 297(3–4), 341–354. https://doi.org/10.1016/j.epsl.2010.06.036
- Long, M. D., & Silver, P. G. (2009). Shear wave splitting and mantle anisotropy: Measurements, interpretations, and new directions. Surveys in Geophysics, 30(4–5), 407–461. https://doi.org/10.1007/s10712-009-9075-1
- Lough, A. C., Wiens, D. A., Barcheck, G. C., Anandakrishnan, S., Aster, R. C., Blankenship, D. D., et al. (2013). Seismic detection of an active subglacial magmatic complex in Marie Byrd Land. Antarctica. *Nature Geoscience*, 6(12). https://doi.org/10.1038/ngeo1992
- Lucas, E. M., Accardo, N. J., Nyblade, A., Lloyd, A. J., Aster, R. C., Wiens, D. A., et al. (2020). Upper mantle seismic anisotropy of Antarctica from shear wave splitting analysis. AGU Fall Meeting
- Lucas, E. M., Soto, D., Nyblade, A. A., Lloyd, A. J., Aster, R. C., Wiens, D. A., et al. (2020). P-and S-wave velocity structure of central West Antarctica: Implications for the tectonic evolution of the West Antarctic Rift System. Earth and Planetary Science Letters, 546, 116437. https://doi.org/10.1016/j.epsl.2020.116437
- Lynner, C., Beck, S. L., Zandt, G., Porritt, R. W., Lin, F.-C., & Eilon, Z. C. (2018). Midcrustal deformation in the Central Andes constrained by radial anisotropy. *Journal of Geophysical Research: Solid Earth*, 123, 4798–4813. https://doi.org/10.1029/2017JB014936
- Mooney, W. D., & Kaban, M. K. (2010). The North American upper mantle: Density, composition, and evolution. *Journal of Geophysical Research: Solid Earth*, 115. https://doi.org/10.1029/2010jb000866
- Moschetti, M., Ritzwoller, M., Lin, F., & Yang, Y. (2010b). Seismic evidence for widespread western-US deep-crustal deformation caused by extension. *Nature*, 464(7290), 885–889. https://doi.org/10.1038/nature08951
- Moschetti, M., Ritzwoller, M., Lin, F.-C., & Yang, Y. (2010a). Crustal shear wave velocity structure of the western United States inferred from ambient seismic noise and earthquake data. *Journal of Geophysical Research*, 115(B10). https://doi.org/10.1029/2010JB007448
- Movaghari, R., JavanDoloei, G., Yang, Y., Tatar, M., & Sadidkhouy, A. (2021). Crustal radial anisotropy of the Iran Plateau inferred from ambient noise tomography. *Journal of Geophysical Research: Solid Earth*, 126, e2020JB020236. https://doi.org/10.1029/2020JB020236
- O'Donnell, J. P., Brisbourne, A. M., Stuart, G. W., Dunham, C. K., Yang, Y., Nield, G. A., et al. (2019). Mapping crustal shear wave velocity structure and radial anisotropy beneath West Antarctica using seismic ambient noise. *Geochemistry, Geophysics, Geosystems*, 20(11), 5014–5037. https://doi.org/10.1029/2019gc008459
- Paxman, G. J. G., Jamieson, S. S. R., Ferraccioli, F., Jordan, T. A., Bentley, M. J., Ross, N., et al. (2019). Subglacial geology and geomorphology of the pensacola-Pole Basin, East Antarctica. *Geochemistry, Geophysics, Geosystems*, 20(6), 2786–2807. https://doi.org/10.1029/2018gc008126
- Phillips, E. H., Sims, K. W., Blichert-Toft, J., Aster, R. C., Gaetani, G. A., Kyle, P. R., et al. (2018). The nature and evolution of mantle upwelling at Ross Island, Antarctica, with implications for the source of HIMU lavas. *Earth and Planetary Science Letters*, 498, 38–53. https://doi.org/10.1016/j.epsl.2018.05.049
- Pourpoint, M., Wiens, D. A., Shen, W., Aster, R. C., Nyblade, A. A., & Wilson, T. J. (2019). Constraints on shallow subglacial structure beneath Thwaites Glacier from joint inversion of receiver function and surface wave data. AGU Fall Meeting.
- Pyle, M. L., Wiens, D. A., Nyblade, A. A., & Anandakrishnan, S. (2010). Crustal structure of the Transantarctic Mountains near the Ross Sea from ambient seismic noise tomography. *Journal of Geophysical Research: Solid Earth*, 115. https://doi.org/10.1029/2009JB007081
- Ramirez, C., Nyblade, A., Emry, E. L., Julià, J., Sun, X., Anandakrishnan, S., et al. (2017). Crustal structure of the Transantarctic Mountains, Ellsworth Mountains and Marie Byrd Land, Antarctica: Constraints on shear wave velocities, Poisson's ratios and Moho depths. *Geophysical Journal International*, 211(3), 1328–1340. https://doi.org/10.1093/gji/ggx333
- Ramirez, C., Nyblade, A., Hansen, S. E., Wiens, D. A., Anandakrishnan, S., Aster, R. C., et al. (2016). Crustal and upper-mantle structure beneath ice-covered regions in Antarctica from S-wave receiver functions and implications for heat flow. *Geophysical Journal International*, 204(3), 1636–1648. https://doi.org/10.1093/gji/ggv542
- Randall, D. E., & Niocaill, C. M. (2004). Cambrian palaeomagnetic data confirm a Natal Embayment location for the Ellsworth-Whitmore Mountains, Antarctica, in Gondwana reconstructions. Geophysical Journal International, 157(1), 105–116. https://doi.org/10.1111/j.1365-246x.2004.02192.x
- Ritzwoller, M. H., & Levshin, A. L. (1998). Eurasian surface wave tomography: Group velocities. *Journal of Geophysical Research*, 103(B3), 4839–4878. https://doi.org/10.1029/97jb02622
- Ritzwoller, M. H., Shapiro, N. M., Levshin, A. L., & Leahy, G. M. (2001). Crustal and upper mantle structure beneath Antarctica and surrounding oceans. *Journal of Geophysical Research: Solid Earth*, 106(B12), 30645–30670. https://doi.org/10.1029/2001JB000179
- Sabra, K. G., Gerstoft, P., Roux, P., Kuperman, W. A., & Fehler, M. C. (2005). Extracting time-domain Green's function estimates from ambient seismic noise. Geophysical Research Letters, 32. https://doi.org/10.1029/2004gl021862
- Schimmel, M., & Gallart, J. (2007). Frequency-dependent phase coherence for noise suppression in seismic array data. *Journal of Geophysical Research*, 112. https://doi.org/10.1029/2006jb004680
- Schimmel, M., & Paulssen, H. (1997). Noise reduction and detection of weak, coherent signals through phase-weighted stacks. *Geophysical Journal International*, 130(2), 497–505. https://doi.org/10.1111/j.1365-246x.1997.tb05664.x
- Shen, W., & Ritzwoller, M. H. (2016). Crustal and uppermost mantle structure beneath the United States. *Journal of Geophysical Research: Solid Earth*, 121, 4306–4342. https://doi.org/10.1002/2016jb012887
- Shen, W., Ritzwoller, M. H., Kang, D., Kim, Y., Lin, F.-C., Ning, J., et al. (2016). A seismic reference model for the crust and uppermost mantle beneath China from surface wave dispersion. *Geophysical Journal International*, 206(2), 954–979. https://doi.org/10.1093/gij/ggw175

ZHOU ET AL. 22 of 23



- Shen, W., Ritzwoller, M. H., & Schulte-Pelkum, V. (2013). A 3-D model of the crust and uppermost mantle beneath the Central and Western US by joint inversion of receiver functions and surface wave dispersion. *Journal of Geophysical Research: Solid Earth*, 118, 262–276. https://doi.org/10.1029/2012jb009602
- Shen, W., Ritzwoller, M. H., Schulte-Pelkum, V., & Lin, F.-C. (2013). Joint inversion of surface wave dispersion and receiver functions: A Bayesian Monte-Carlo approach. *Geophysical Journal International*, 192(2), 807–836. https://doi.org/10.1093/gji/ggs050
- Shen, W., Wiens, D., Lloyd, A., & Nyblade, A. (2020). A geothermal heat flux map of Antarctica empirically constrained by seismic structure. Geophysical Research Letters, 47, e2020GL086955. https://doi.org/10.1029/2020GL086955
- Shen, W., Wiens, D. A., Anandakrishnan, S., Aster, R. C., Gerstoft, P., Bromirski, P. D., et al. (2018). The Crust and upper mantle structure of central and west Antarctica from bayesian inversion of Rayleigh wave and receiver functions. *Journal of Geophysical Research*, 123, 7824–7849. https://doi.org/10.1029/2017JB015346
- Shen, W., Wiens, D. A., Stern, T., Anandakrishnan, S., Aster, R. C., Dalziel, I., et al. (2018). Seismic evidence for lithospheric foundering beneath the southern Transantarctic Mountains, Antarctica. *Geology*, 46(1), 71–74. https://doi.org/10.1130/G39555.1
- Siddoway, C. S. (2007). Tectonics of the West Antarctic rift system: New light on the history and dynamics of distributed intracontinental extension (pp. 91–114). National Academies Press. https://doi.org/10.3133/ofr20071047kp09
- Stern, T. A., & Brink, U. S. (1989). Flexural uplift of the Transantarctic Mountains. Journal of Geophysical Research, 94(B8), 10315–10330. https://doi.org/10.1029/ib094ib08p10315
- Tankersley, M., Siddoway, C. S., Horgan, H. J., Tontini, F. C., & Tinto, K. J. (2021). New contribution to Ross Ice Shelf (Antarctica) boundary conditions: Basement depths and sediment thickness determined from aeromagnetic data. AGU Fall Meeting.
- ten Brink, U., & Stern, T. (1992). Rift flank uplifts and Hinterland Basins: Comparison of the Transantarctic Mountains with the Great Escarpment of southern Africa. *Journal of Geophysical Research*, 97(B1), 569. https://doi.org/10.1029/91jb02231
- Vincenty, T. (1975). Direct and inverse solutions of geodesics on the ellipsoid with application of nested equations. *Survey Review*, 23(176), 88–93. https://doi.org/10.1179/sre.1975.23.176.88
- Wang, K., Jiang, C., Yang, Y., Schulte-Pelkum, V., & Liu, Q. (2020). Crustal deformation in southern California constrained by radial anisotropy from ambient noise adjoint tomography. *Geophysical Research Letters*, 47. https://doi.org/10.1029/2020gl088580
- Wannamaker, P., Hill, G., Stodt, J., Maris, V., Ogawa, Y., Selway, K., et al. (2017). Uplift of the central transantarctic mountains. *Nature Communications*, 8(1), 1588. https://doi.org/10.1038/s41467-017-01577-2
- Watson, T., Nyblade, A., Wiens, D. A., Anandakrishnan, S., Benoit, M., Shore, P. J., et al. (2006). P and S velocity structure of the upper mantle beneath the Transantarctic Mountains, East Antarctic craton, and Ross Sea from travel time tomography: Mantle P and S velocity structure. *Geochemistry, Geophysics, Geosystems*, 7(7). https://doi.org/10.1029/2005gc001238
- White-Gaynor, A. L., Nyblade, A. A., Aster, R. C., Wiens, D. A., Bromirski, P. D., Gerstoft, P., et al. (2019). Heterogeneous upper mantle structure beneath the Ross Sea Embayment and Marie Byrd Land, West Antarctica, revealed by P-wave tomography. *Earth and Planetary Science Letters*, 513, 40–50, https://doi.org/10.1016/j.epsl.2019.02.013
- Wiens, D. A., Shen, W., & Lloyd, A. J. (2021). The seismic structure of the antarctic upper mantle (Vol. 56, pp. 9–2020). Geological Society of London. June 2021. https://doi.org/10.1144/M56-2020-18
- Wilgus, J., Jiang, C., & Schmandt, B. (2020). A middle crustal channel of radial anisotropy beneath the northeastern basin and range. *Tectonics*, 39(7). https://doi.org/10.1029/2020tc006140
- Wilson, D. S., & Luyendyk, B. P. (2006). Bedrock platforms within the Ross Embayment, West Antarctica: Hypotheses for ice sheet history, wave erosion, Cenozoic extension, and thermal subsidence. *Geochemistry, Geophysics, Geosystems*, 7(12). https://doi.org/10.1029/2006gc001294
- Wobbe, F., Lindeque, A., & Gohl, K. (2014). Anomalous South Pacific lithosphere dynamics derived from new total sediment thickness estimates off the West Antarctic margin. *Global and Planetary Change*, 123, 139–149. https://doi.org/10.1016/j.gloplacha.2014.09.006
- Wörner, G. (1999). Lithospheric dynamics and mantle sources of alkaline magmatism of the Cenozoic West Antarctic Rift System. *Global and Planetary Change*, 23(1–4), 61–77. https://doi.org/10.1016/s0921-8181(99)00051-x
- Xie, J., Ritzwoller, M. H., Shen, W., Yang, Y., Zheng, Y., & Zhou, L. (2013). Crustal radial anisotropy across Eastern Tibet and the Western Yangtze Craton. *Journal of Geophysical Research: Solid Earth*, 118, 4226–4252. https://doi.org/10.1002/jgrb.50296
- Zhu, H., Komatitsch, D., & Tromp, J. (2017). Radial anisotropy of the North American upper mantle based on adjoint tomography with USArray. Geophysical Journal International, 211(1), 349–377. https://doi.org/10.1093/gji/ggx305

ZHOU ET AL. 23 of 23